

Synergizing Fe₂O₃ nanoparticles on single atom Fe-N-C for nitrate reduction to ammonia at industrial current densities

Eamonn Murphy^{1†}, Baiyu Sun^{1†}, Martina Rüscher², Yuanchao Liu¹, Wenjie Zang³, Shengyuan Guo¹, Uta Hejral², Ying Huang³, Alvin Ly³, Iryna V. Zenyuk¹, Xiaoqing Pan³, Janis Timoshenko², Beatriz Roldán Cuenya², Erik D. Spoecker⁴ and Plamen Atanassov^{1*}

¹Department of Chemical and Biomolecular Engineering, National Fuel Cell Research Center, University of California, Irvine, California 92697, USA

²Department of Interface Science, Fritz-Haber-Institut der Max-Planck-Gesellschaft, 14195 Berlin, Germany

³Department of Materials Science and Engineering, University of California, Irvine, California 92697, USA

⁴Sandia National Laboratories, Albuquerque, New Mexico 87185, USA

†Authors contributed equally

*Corresponding author: plamen.atanassov@uci.edu

Abstract

The electrochemical reduction of oxidized nitrogen species enables a pathway for the carbon neutral synthesis of ammonia (NH₃). The most oxidized form of nitrogen, nitrate (NO₃⁻) can be reduced to NH₃ via the nitrate reduction reaction (NO₃RR), which has been demonstrated at high selectivity. However, to make NH₃ synthesis cost-competitive with current technologies, high NH₃ partial current densities (j_{NH_3}) must be achieved to reduce the levelized cost of NH₃. Here, we leverage the high NO₃RR activity of Fe-based materials to synthesize a novel active particle-active support system with Fe₂O₃ nanoparticles supported on atomically dispersed Fe-N-C. By synergizing the activity of both nanoparticles and single atom sites, the optimized 3xFe₂O₃/Fe-N-C catalyst demonstrates an ultrahigh NO₃RR activity, reaching a maximum j_{NH_3} of 1.95 A cm⁻² at a Faradaic efficiency (FE) for NH₃ of 100% and an NH₃ yield rate over 9 mmol hr⁻¹ cm⁻². Operando XANES and post-mortem XPS reveal the importance of a pre-reduction activation step, reducing the surface Fe₂O₃ (Fe³⁺) to highly active Fe⁰ sites, which are maintained during electrolysis, to realize the ultrahigh NO₃RR activity. Durability studies demonstrate the robustness of both the Fe₂O₃ particles and Fe-N_x sites at highly cathodic potentials, maintaining a current of -1.3 A cm⁻² over 24 hours, a near unity FE_{NH₃}. This work exhibits an effective and durable active particle-

active support system enhancing the performance of the NO₃RR, enabling industrially relevant current densities and near 100% selectivity.

Keywords: Nitrate reduction, nitrite reduction, ammonia, alkaline, single atom catalyst, active support, iron oxide, operando XAS

Introduction

The synthesis of ammonia (NH₃) based fertilizers is essential to support the growing global food demands. Currently, thermochemical NH₃ synthesis via the Haber Bosch (HB) process, accounts for approximately of 2% of global energy usage and more than 1.4% of global CO₂ emissions.^{1–3} The electrochemical reduction of di-nitrogen (N₂) is a theoretically ideal NH₃ synthesis pathway, however, activation of the highly stable and insoluble (in protic electrolytes) N₂ molecule remains challenging and unproven.^{4,5} As an alternative for the N₂ molecule, recently there has been a revitalized interest in the more oxidized form of nitrogen, nitrate (NO₃⁻). Nitrate is an environmental pollutant present in ground water runoffs due to heavy overfertilization practices and in industrial waste streams at varying concentrations (0.001 – 2M).^{6,7} The reduction of NO₃⁻ to NH₃ is appealing to reutilize waste nitrogen into value added NH₃, alleviating the demand on the HB process, while also serving as an alternative to traditional denitrification techniques, providing dual benefits for the nitrate reduction reaction (NO₃RR). It should be noted that the NO₃RR alone is not a replacement for the HB process, because typically, the nitrogen atom in the NO₃⁻ originates from a HB produced NH₃, but the NO₃RR can help to enhance the efficiency of the N-cycle.⁸ Or the NO₃RR can be coupled with N₂ plasma oxidation processes to be totally decouple from the HB process.

Electrochemically, the NO₃RR is a complex 8e⁻ transfer reaction, consisting of several possible soluble and insoluble intermediates (NO₂, NO₂⁻, NO, N₂, N₂O, NH₂OH, NH₃, and N₂H₄) and competes directly with the hydrogen evolution reaction (HER).⁹ Aiming at industrial relevance, it is essential to optimize both catalyst activity and selectivity towards a singular product, in this discussion, NH₃. In practice, the use of an alkaline media (pH 13-14) can enhance the NO₃RR current throughput (over most metals) and significantly suppresses the formation of the common 2e⁻ side product, nitrite (NO₂⁻), often reporting the highest NH₃ Faradaic efficiencies (FE_{NH3}) and yield rates (Yield_{NH3}) as shown in Table S1.^{10–12}

When targeting industrially relevant current densities, there is a competing compromise between the energy efficiency and NH_3 partial current density (j_{NH_3}), both of which are influenced by the applied cathodic potential and corresponding NH_3 selectivity. In alkaline media, the standard reduction potential for the NO_3RR to NH_3 (equation 1) is 0.69V vs. RHE.^{10,13}



Currently, several reports achieve high FE_{NH_3} pushing upwards of 90%, some at mildly reductive potentials, resulting in relatively high cathodic energy efficiencies, ca. 40%.^{10,14–17} However, most of these reports suffer from limited j_{NH_3} (0.5 – 80 mA cm^{-2}), resulting in the need for largely scaled up devices or stacks and thus intensive capital costs of these systems. In contrast, the NO_3RR systems with higher j_{NH_3} ($80 < X \text{ mA cm}^{-2}$) relied on more cathodic overpotentials, suffering from largely reduced energy efficiencies (e.g., below 30%).^{18–20} Establishing a tradeoff between energy efficiency and j_{NH_3} remains ambiguous, although, a recent economic analysis quantifying the levelized cost of NH_3 , suggested that the j_{NH_3} (production rate) has a more significant influence than the cell voltage or electricity price in reducing the levelized cost of NH_3 .²⁰

Cost efficient platinum-group-metal free (PGM-free) metals typically require more cathodic potentials to achieve a desirable j_{NH_3} . One way to achieve higher energy efficiency is to utilize PGMs and their alloys as these metals often have earlier (closer to the thermodynamic) reaction onset potentials. However, as more cathodic potentials are applied to achieve higher j_{NH_3} , they are typically out competed by the HER.^{11,21} However, due to their scarcity and price, large scale systems based on PGMs are not economically feasible. Interestingly, a strategy currently being investigated for the oxygen reduction reaction (ORR) is the use of active supports to increase the activity and durability of the catalyst systems.^{22–24} Where a typical inert carbon support (Vulcan / carbon black) is replaced with an ORR active, atomically dispersed metal-nitrogen-carbon (M-N-C) support, often Fe-N-C or Co-N-C. It's speculated that possible electron donation between the platinum nanoparticles and the M-N-C can create more favorable intermediate adsorption energies, increasing the activity. Additionally, it was suggested the M-N₄ active site can modify the electronic structure of the neighboring carbon, increasing the stability of the nanoparticles.

It has been shown in our previous works and complemented by other studies that atomically dispersed Fe-N-C is highly active for the NO_3RR , achieving a FE_{NH_3} greater than 90%.^{10,25–27} This work builds upon of the high NO_3RR activity of Fe-N-C catalysts and utilizes it as an active-support for Fe_2O_3 nanoparticles, synthesizing a $\text{Fe}_2\text{O}_3/\text{Fe-N-C}$ system for ultra-high NO_3RR to

NH₃ performance. Specifically, the 3xFe₂O₃/Fe-N-C catalyst exhibits a potential independent selectivity (~100% FE_{NH₃}) between -0.4 to -1.2 V vs. RHE, while increasing the j_{NH₃} up to nearly 2 A/cm² (at a Yield_{NH₃} of more than 9 mmol_{NH₃} hr⁻¹ cm⁻²). Operando XANES supported by post-mortem XPS reveal that the pre-reduction activation step is critical in achieving the ultrahigh NO₃RR performance, generating highly active, surface Fe⁰ sites. A durability test showed that the optimized 3xFe₂O₃/Fe-N-C catalyst could maintain a FE_{NH₃} between 90-100% at a current of 1.3 A/cm² for over 24-hours, demonstrating the durability of utilizing an active-catalyst/active-support system.

Results and discussion

Fe₂O₃/Fe-N-C synthesis and characterization

Fe₂O₃ nanoparticles supported on atomically dispersed Fe-N-C (Fe₂O₃/Fe-N-C) were synthesized by utilizing the sacrificial support method (SSM) for the Fe-N-C, followed by an organic solvent synthesis method for the Fe₂O₃ nanoparticles. The SSM is a robust technique developed by our group for the synthesis of atomically dispersed M-N-C catalysts.²⁶ Schematically, the SSM is shown in Figure 1a, wherein a catalyst slurry of a carbon-nitrogen precursor is mixed with nano porous silica and an iron-nitrate salt. The precursor mixture then undergoes a series of ball milling, pyrolyzing and acid etching steps, yielding an exclusively atomically dispersed Fe-N-C support.²⁶ Afterwards, the Fe₂O₃ nanoparticles were synthesized on either a Vulcan-XC72 or Fe-N-C support, utilizing an organic solvent method. The HAADF-STEM image (Figure 1b) and TEM images (Figure S1) show a homogenous dispersion of the Fe₂O₃ nanoparticles with well-controlled sub-5 nm diameter. Additionally, the corresponding elemental mapping is shown in Figure 1b, for the Fe₂O₃/XC72 catalyst with a homogenous distribution of Fe, O and C. The Fe₂O₃ nanoparticles have a spinel-like structure, typical of gamma-phase Fe₂O₃, as observed in the aberration corrected (AC) HAADF-STEM image in Figure 1c. A schematic of the Fe₂O₃ spinel crystal structure is given in Figure 1d. The high magnification STEM image and energy dispersive x-ray spectroscopy (EDS) mapping in Figure 1e, verify the atomic dispersion of Fe and N-doping in the Fe-N-C support. After reducing the Fe₂O₃ nanoparticles on to the Fe-N-C support, Figure 1f confirms that the Fe-N-C support retains its atomic dispersion as single atom Fe sites, clearly co-existing with the Fe₂O₃ nanoparticles. The corresponding EDS mapping of the Fe₂O₃/Fe-N-C catalyst in Figure 1g, confirms the presence of nitrogen from the Fe-N-C support. The crystal structure of the catalyst was examined by X-ray diffraction (XRD), confirming the formation of Fe₂O₃ (Figure S2). As a comparison to the Fe₂O₃ catalyst, CoO_x and RuO_x were also synthesized analogously and

characterized using TEM and XRD (Figure S3-S4). Furthermore, Raman spectroscopy was performed on Fe-N-C and XC72 supports, showing similar graphitic content between the catalyst supports, Figure S5.

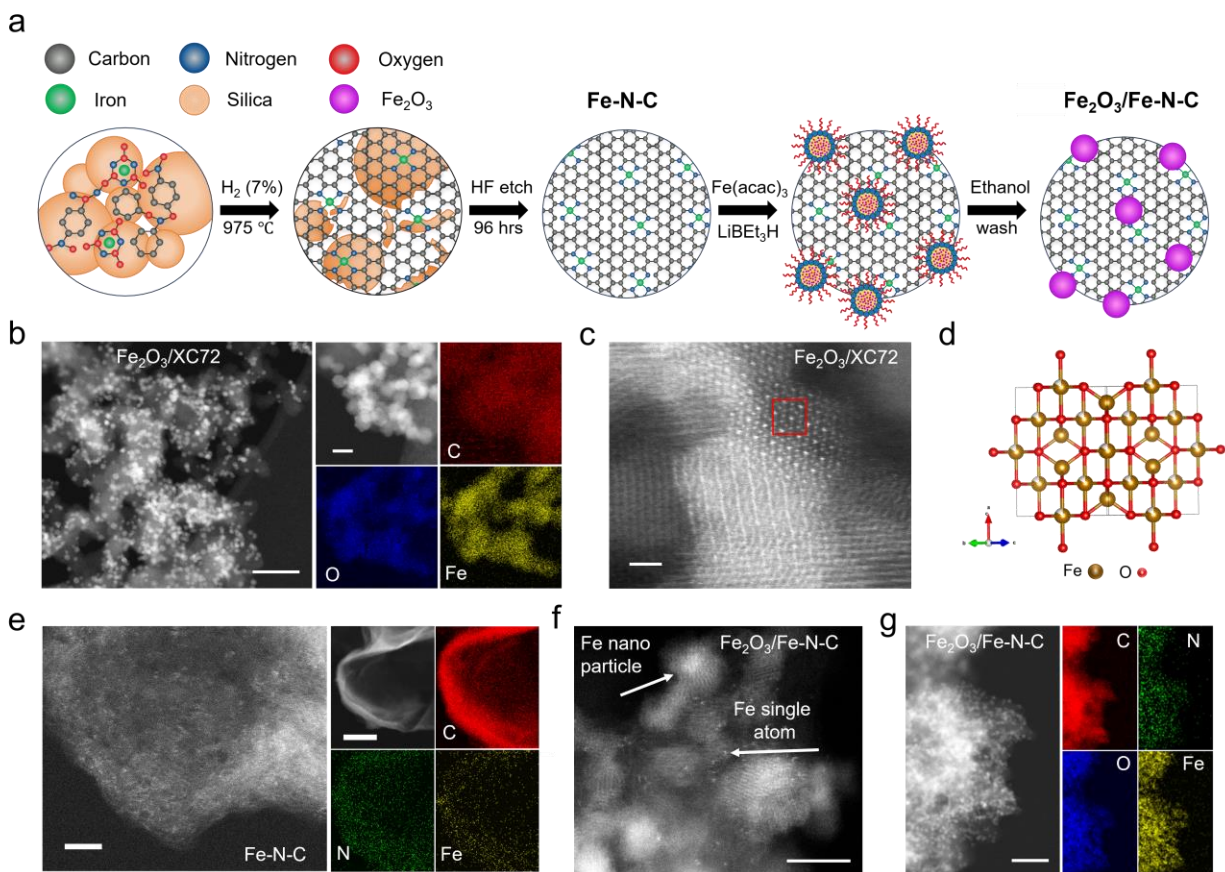


Figure 1. Synthesis schematic and AC-HAADF-STEM images of the Fe_2O_3 based catalysts. (a) Synthesis schematic, utilizing the sacrificial support method and an organic solvent synthesis to deposit Fe_2O_3 nanoparticles on the atomically dispersed Fe-N-C. (b) STEM images of the Fe_2O_3 catalyst supported on XC72 carbon, the scale bar is 50 nm, with its corresponding EDS mapping, scale bar is 5 nm. (c) Atomic resolution STEM image showing the Fe_2O_3 spinel structure, scale bar is 2 nm. (d) Schematic representation of the Fe_2O_3 spinel crystal structure, created using VESTA. (e) Atomic resolution STEM image of the atomically dispersed Fe-N-C catalyst support, with its corresponding EDS mapping, scale bar is 2 nm. (f) Atomic resolution STEM image showing the Fe_2O_3 nanoparticles supported on the atomically dispersed Fe-N-C, scale bar is 5 nm. (g) EDS mapping of the $\text{Fe}_2\text{O}_3/\text{Fe-N-C}$ catalyst, scale bar is 50 nm.

To evaluate the chemical state of the $\text{Fe}_2\text{O}_3/\text{Fe-N-C}$ catalyst and the potential electronic structure changes triggered by interactions between Fe-N_x sites and Fe_2O_3 nanoparticles, atomic resolution electron energy loss spectroscopy (EELS), X-ray absorption spectroscopy (XAS) and X-ray photoelectron spectroscopy (XPS) were utilized. EELS was used to probe the

valence state of the single-atom Fe and the Fe₂O₃ sites. Figure 2a shows the locations where EELS spectra were taken for Fe₂O₃ particles (locations 1 and 2) and single atom Fe sites (locations 3 and 4). Both spectra show the Fe-L_{3,2} edges, however, there is an L₃, L₂ excitation edge shift to lower energy loss and reduced L₃/L₂ white line ratio for single atom Fe (peak spacing of 12.4 eV), compared to Fe₂O₃ (13.2 eV) in Figure 2b. This energy shift and quantitative analysis of the Fe- L₃/L₂ edges suggest the single atom Fe to be in an oxidation state lower than Fe³⁺, in agreement with our previous work where Fe-N-C has an oxidation state *ca.* Fe^{2.6+}.²⁶ At the same time, the analysis for the Fe₂O₃ nanoparticles indicated an oxidation state of Fe³⁺, in agreement with the XAS and XPS (Figure S6) results. Atomic resolution EELS was further applied for a highly localized evaluation of possible Fe₂O₃ and Fe-N_x interactions modifying the electronic structure of the nanoparticles. Comparing the Fe-L_{3,2} edges of the Fe₂O₃ nanoparticles supported on Fe-N-C or XC72 reveals a 0.1 eV shift in the energy loss, Figure 2c. Such small shifts in energy loss can arise due to experimental conditions and inaccuracies in the selected method for spectra processing (something which requires extreme care and is system dependent).²⁸ Therefore, further complementary techniques are employed to evaluate possible nanoparticle-single atom interactions.

X-ray absorption near edge structure (XANES) of the Fe K-edge (7112 eV) was employed to investigate the chemical state of the Fe₂O₃ nanoparticles on both supports, Figure 2d. The Fe K-edge XANES spectra for both Fe₂O₃ catalysts again confirm that Fe is in a Fe³⁺ oxidation state. The XANES spectra for the catalysts are in between those for the γ-Fe₂O₃ and α-Fe₂O₃ references. We thus further refer to these Fe species simply as Fe₂O₃. Note that our previous work, utilizing the same Fe-N-C suggests the Fe-N_x sites to be in a *ca.* Fe^{2.6+} oxidation state.²⁶ Again, to evaluate possible Fe₂O₃ (Fe³⁺) and Fe-N_x (Fe^{~2.6+}) interactions, the rising edge and pre-edge of the Fe₂O₃ supported on Fe-N-C and XC72 were compared, as shown in Figure 2e, however, no meaningful shifts in the energy were observed. The local coordination of Fe species was further analyzed by Fourier transformed extended X-ray adsorption fine structure (FT-EXAFS) in Figure 2f. For the Fe₂O₃ catalysts, regardless of the support, two dominating peaks are observed. One at a low bond distance (*ca.* 1.4 Å, phase uncorrected), corresponding to the expected Fe-O coordination and one at larger bond distance (*ca.* 2.6 Å, phase uncorrected), which corresponds to the Fe-Fe coordination in Fe₂O₃, and is in agreement with the Fe-oxide reference materials. As shown in our previous work, the EXAFS for the Fe-N-C supports exhibits only one peak at low bond distance for Fe-N, confirming its atomically dispersed nature.²⁶ The corresponding EXAFS k-space analysis is shown in Figure S7.

To further investigate the chemical environment and coordination of the Fe species, XPS was performed. Figure 2h shows the N 1s spectra for the Fe₂O₃/Fe-N-C catalyst, confirming the Fe-N_x coordination, along with the (NO₃RR active) pyridinic and pyrrolic N-moieties, characteristic of the Fe-N-C support (XPS for the Fe-N-C support is given in Figure S8). From the deconvoluted Fe 2p spectra in Figure 2i, the oxidation state of Fe₂O₃ is Fe³⁺, regardless of the support used, further corroborating the EELS and XANES analysis. Full XPS deconvolution of the C 1s, O 1s, N 1s and Fe 2p spectra for the Fe₂O₃/Fe-N-C and Fe₂O₃/XC72 catalysts are shown in Figure S6 and S9, respectively. Again, to elucidate possible particle-single atom interactions, the Fe 2p spectra between the Fe₂O₃ supported on Fe-N-C and XC72 were compared, Figure 2j, a binding energy shift of *ca.* 0.2 eV is observed, comparable to that of recent nanoparticle-single atom reports in the literature.^{29–31} However, binding energy shifts during the deconvolution and calibration (commonly to features in C 1s spectrum) of the spectra, can easily induce binding energy shifts on the level of 0.2 eV, especially when the complex nature of the carbon is changing in the compared catalyst supports.³²

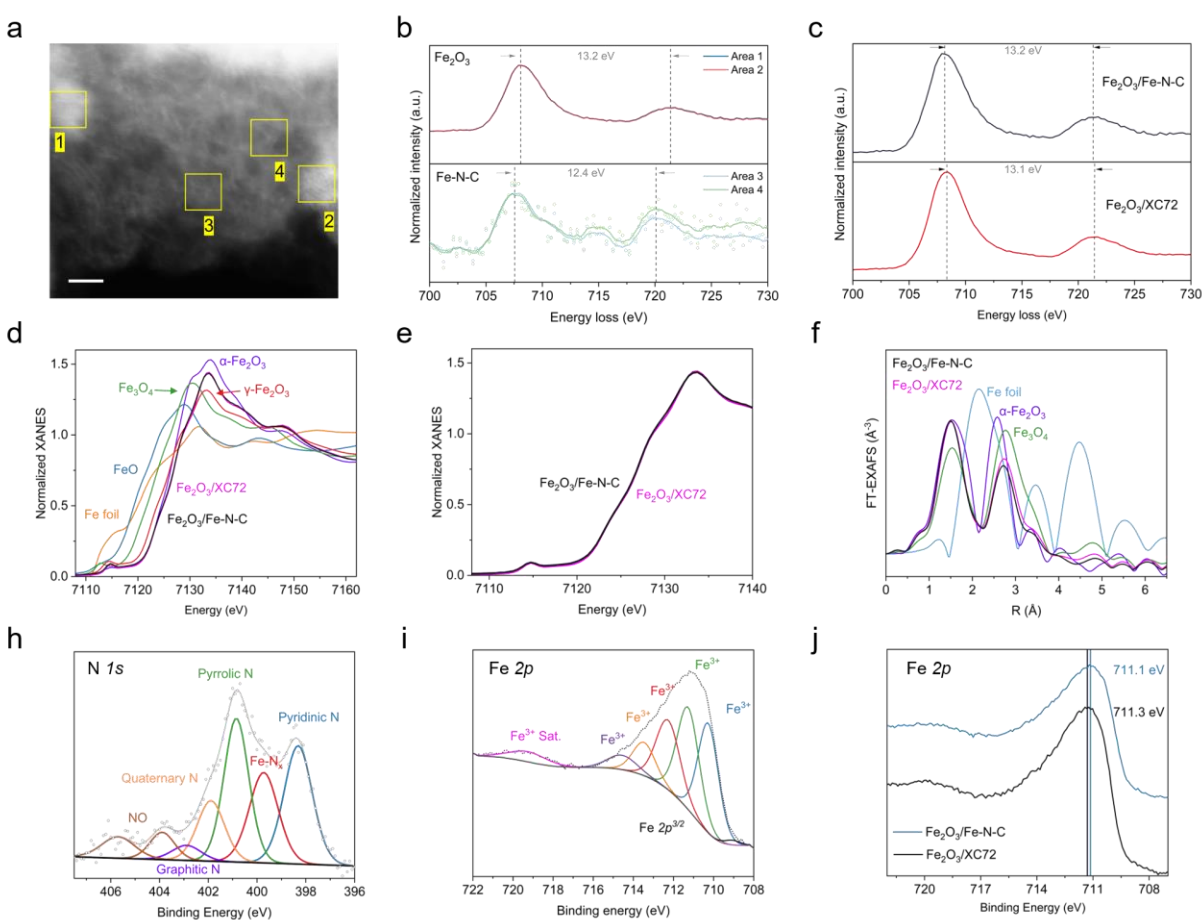


Figure 2. Local chemical and coordination environment of the Fe₂O₃ nanoparticle catalysts. (a) AC-STEM image and EELS spectra locations on the Fe₂O₃/Fe-N-C catalysts, scale bar is 2 nm. (b) EELS spectra of the Fe-L_{3,2} edges of the Fe₂O₃ nanoparticle (top) and atomically dispersed Fe-N_x sites (bottom). (c) EELS spectra comparing the energy loss of the Fe-L_{3,2} edge of the Fe₂O₃ supported on Fe-N-C or XC72. Fe K-edge XAS data for the Fe₂O₃ catalysts supported on both Fe-N-C and XC72 (d) XANES spectra with the corresponding references and (e) XANES spectra comparing Fe₂O₃ supported on XC72 vs. Fe-N-C. (f) Fourier transformed EXAFS of the Fe₂O₃/Fe-N-C catalyst and corresponding references. XPS spectra for the Fe₂O₃/Fe-N-C catalyst (h) N 1s spectra and (i) Fe 2p XPS spectra. (j) Comparison of the Fe 2p XPS spectra for the Fe₂O₃ catalyst supported on Fe-N-C or XC72.

It should be noted that as the popularity of nanoparticle/single atom support systems increases, extreme care must be taken in the interpretation of chemical state characterizations. Often nanoparticle/single atom support electronic interactions are claimed exclusively through ambiguous shifts in the XPS spectra, and subsequently used as the foundation for interesting computational models and reactions mechanisms and attributed to any increased activity and stability. In this work, after rigorously investigating the electronic structure of the Fe₂O₃ supported on atomically dispersed Fe-N-C and XC72 supports, with highly localized and more bulk techniques (EELS, XAS and XPS), no spectroscopically detected interactions were observed. Critically, however, this does not rule out the possibility of electronic interactions between the Fe₂O₃ nanoparticles and Fe-N_x sites enhancing NO₃RR performance. These highly sensitive interactions might require probing through electrochemical processes, in which the nanoparticle is active, while M-N_x site is inert, allowing changes in onset potentials or peak shapes to reflect interactions between the nanoparticle and M-N_x site (*ie.* CO stripping on Pt/M-N-C). Regardless, a Fe₂O₃/Fe-N-C active particle-active support catalyst has been synthesized and robustly characterized. The Fe₂O₃/Fe-N-C catalyst contains a multitude of highly active NO₃RR sites at both the nanoparticle and single atom scales, which are synergized, enhancing the NO₃RR performance.

Electrochemical NO₃RR performance

Linear sweep voltammetry (LSV) was performed in an alkaline, 1M KOH + 0.16M KNO₃ electrolyte to assess the NO₃RR activity of the blank carbon paper, XC72 and Fe-N-C catalyst supports, and the Fe₂O₃ nanoparticles supported on both XC72 and Fe-N-C as shown in Figure 3a. From the LSV there is a slight positive shift in the reaction onset potential (-0.59 V vs. RHE) in comparison to the blank carbon paper electrode, when using XC72, indicating even the metal-free carbon support has some, albeit limited NO₃RR performance. Note in this work all potentials are reported against the reversible hydrogen electrode, RHE. Employing the Fe-N-C

catalyst support realizes a significant positive shift in the reaction onset potential (-0.34 V). Interestingly, despite having increased j_{NH_3} at higher overpotentials in alkaline media, the Fe-N-C is observed to have a more positive onset reaction potential in neutral media (0.05M PBS), which could be due to its hyperactivity toward reducing the NO_2^- intermediate in the NO_3RR $2\text{e}^- + 6\text{e}^-$ transfer pathway, often formed at lower pH, which is suppressed in alkaline media.^{25,26} The addition of Fe_2O_3 nanoparticles further shifts the reaction onset potential even more positively to -0.14 V, regardless of either the XC72 or Fe-N-C support. However, at more cathodic potentials, the current of $\text{Fe}_2\text{O}_3/\text{Fe-N-C}$ dominates due to additional activity provided by the active Fe-N_x sites in the Fe-N-C support. Figure S10 shows the LSV comparison of the Fe, Co and Ru oxides supported on XC72, where RuO_x shows the most positive onset potential (ca. +0.05 V, however, is quickly out competed by the HER). Figure S3 and S4 show the LSV performance of CoO_x and RuO_x in electrolyte with and without KNO_3 . To evaluate the catalytic performance of the supports towards the NO_3RR , chronoamperometry measurements were performed at potentials between -0.20 and -1.20 V as shown in Figure 3b. The XC72 support has negligible activity until -0.8 V and reaches a maximum FE_{NH_3} of 55%. However, the Fe-N-C support demonstrates superior activity, holding a FE_{NH_3} of ca. 80% above -0.20 V, reaching a maximum of 90% at -0.40 V and a maximum $\text{Yield}_{\text{NH}_3}$ of 2.9 $\text{mmol}_{\text{NH}_3} \text{hr}^{-1} \text{cm}^{-2}$ (at an NH_3 partial current density, $j_{\text{NH}_3} = 490 \text{ mA cm}^{-2}$ at -1.20 V), surpassing other reported Fe-N-C catalysts for the NO_3RR (or 135 mA/cm^2 at -0.6 V).^{10,27} The addition of Fe_2O_3 nanoparticles enhances the FE_{NH_3} (after -0.20 V) and significantly improves the $\text{Yield}_{\text{NH}_3}$ over the potential range reaching a maximum of 6 $\text{mmol}_{\text{NH}_3} \text{hr}^{-1} \text{cm}^{-2}$ ($j_{\text{NH}_3} = 1,265 \text{ mA cm}^{-2}$), Figure 3c. Furthermore, $\text{Fe}_2\text{O}_3/\text{Fe-N-C}$ demonstrates increased FE_{NH_3} and $\text{Yield}_{\text{NH}_3}$ over the potential range compared to $\text{Fe}_2\text{O}_3/\text{XC72}$. Interestingly, the $\text{Fe}_2\text{O}_3/\text{Fe-N-C}$ can maintain a FE_{NH_3} of 90-95% over the potential range, highlighting the catalysts' potential independent NH_3 selectivity, resisting the parasitic HER even at highly cathodic potentials.

Having established the superior performance of the $\text{Fe}_2\text{O}_3/\text{Fe-N-C}$ catalyst, an Fe_2O_3 loading study was performed by adjusting the $\text{Fe}(\text{acac})_3$ loading, to further enhance the NO_3RR activity. The TEM images in Figure 3d show the $\text{Fe}(\text{acac})_3$ loading impact on the Fe_2O_3 site density and gradual formation of agglomerates. With the standard Fe_2O_3 (eg. $1\times\text{Fe}(\text{acac})_3$), a relatively low Fe_2O_3 site density is observed with no agglomerates. The optimal loading appears to be at $3\times\text{Fe}_2\text{O}_3$, at this loading, the Fe_2O_3 site density significantly increases, with slight agglomerate formation beginning, while at $4\times\text{Fe}_2\text{O}_3$, agglomerates dominate, reducing the catalytically active surface area. Thermogravimetric analysis, Figure S11 determined a Fe weight loading of 42% for the $3\times\text{Fe}_2\text{O}_3$ catalyst and 22% for the $1\times\text{Fe}_2\text{O}_3$, indicating a non-linear increase in Fe content

with precursor loading. The optimal $3x\text{Fe}_2\text{O}_3$ loading is directly observed in the NO_3RR performance and calculated ECSA, Figure 3e and Figure S12, respectively. Furthermore, $3x\text{Fe}_2\text{O}_3/\text{Fe-N-C}$ demonstrates the highest FE_{NH_3} maintaining ca. 95-100% from -0.40 to -1.20 V, and highest $\text{Yield}_{\text{NH}_3}$ at all potentials, reaching a maximum of $8.3 \text{ mmol}_{\text{NH}_3} \text{ hr}^{-1} \text{ cm}^{-2}$ ($j_{\text{NH}_3} = 1,785 \text{ mA cm}^{-2}$). To further optimize the catalyst performance and increase j_{NH_3} , the optimal catalyst loading on the carbon paper was investigated. The ink volume of $3x\text{Fe}_2\text{O}_3/\text{Fe-N-C}$ drop cast on the carbon paper electrode was varied to achieve a final catalyst loading between 0.2 – 10.0 mg/cm^2 . LSV was performed to screen the activity of the different catalyst loadings, shown in Figure S13. As the catalyst loading increased from 0.2 – 1.0 mg/cm^2 , the maximum current increases and the reaction onset potential shifts positively, with no improvement being observed between 0.5 – 1.0 mg/cm^2 . However, after 1.0 mg/cm^2 the catalyst layer becomes too thick, inhibiting optimal use of the porous carbon paper, resulting in reduced activity, with 10.0 mg/cm^2 giving the lowest performance. As an activity comparison, Figure S13c shows the reaction onset potential and maximum current at -0.5 V (the maximum potential at which a cathodic energy efficiency of 30% is achieved assuming 100% FE_{NH_3}). The optimal catalyst loading is determined to be 0.5 mg/cm^2 , giving an onset potential of ca. -0.13 V and a current density of 520 mA cm^{-2} at -0.50 V. Therefore, the optimal catalyst is the $3x\text{Fe}_2\text{O}_3/\text{Fe-N-C}$ with a loading of 0.5 mg/cm^2 , and the electrochemical results discussed further in this manuscript utilize these conditions. Finally, to confirm the source of NH_3 originates from the NO_3^- in the electrolyte, rather than contamination or decomposition of the N-doped carbon support, a series of control experiments were performed. Electrolysis from -0.2 to -1.2 V for 15 min each was performed in 1M KOH electrolyte (without NO_3^-) and tested by UV-Vis, showing no detected NH_3 in the absence of NO_3^- , Figure S14a-b. Next, isotopically labeled experiments were performed using a 1M KOH + 0.16M $^{15}\text{KNO}_3$ electrolyte. Electrolysis was performed at -1.0 V for 15 min, and ^1H NMR quantified the $^{15}\text{NH}_3$ produced. The isotopic measurements (Figure S14c-d) show a strong comparison between the non-isotopically doped experiments, both at a FE_{NH_3} ca. 100% and a yield rate of $6.5 \text{ mmol hr}^{-1} \text{ cm}^{-2}$ ($^{15}\text{KNO}_3$) and $6.2 \text{ mmol hr}^{-1} \text{ cm}^{-2}$ ($^{14}\text{KNO}_3$), confirming that any NH_3 detected results from the activation of NO_3^- .

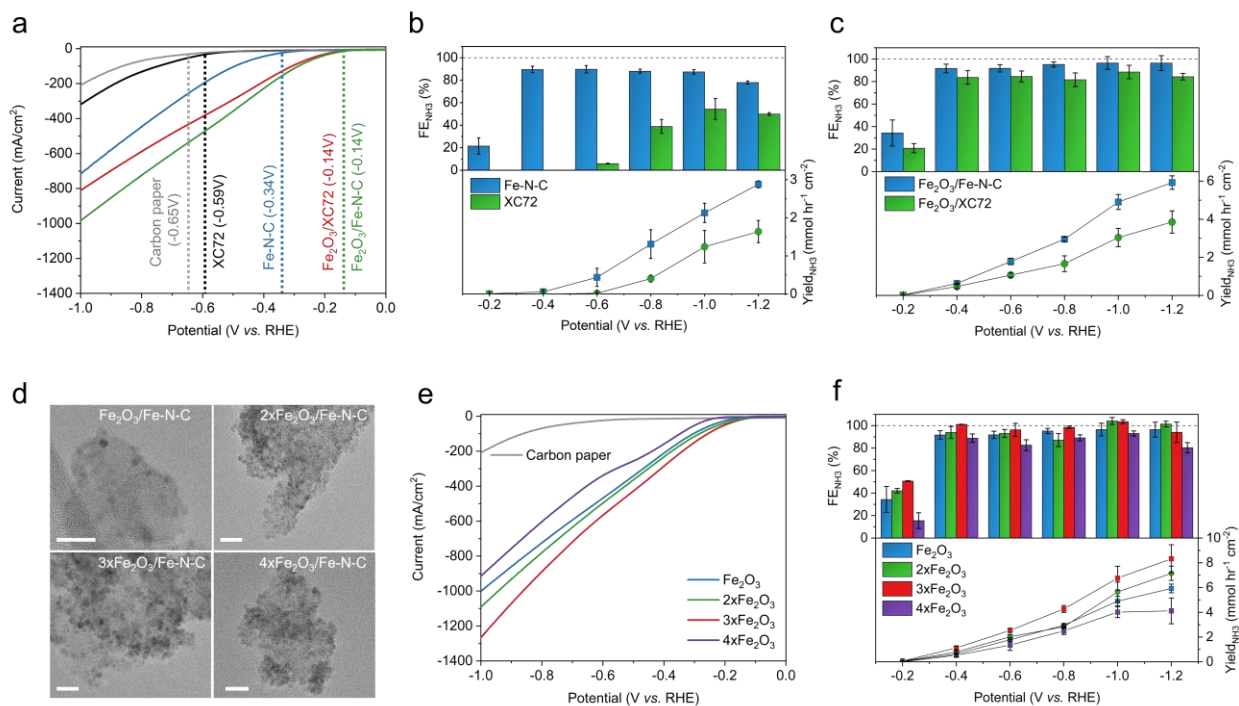


Figure 3. Electrochemical NO₃RR performance of Fe₂O₃ based catalysts and supports in 1M KOH + 0.16M KNO₃ electrolyte. (a) Linear sweep voltammetry at a scan rate of 5 mV/s. The red line is Fe₂O₃/XC72 and the green line is Fe₂O₃/Fe-N-C. Chronoamperometry measurements for 15 min at applied potentials from -0.20 to -1.20 V vs. RHE. (b) comparing XC72 vs. Fe-N-C catalyst supports, (c) comparing Fe₂O₃/Fe-N-C vs. Fe₂O₃/XC72. (d) TEM images of increasing Fe₂O₃ loadings supported on Fe-N-C, the scale bar is 20 nm. Electrochemical performance of Fe₂O₃/Fe-N-C with varying Fe₂O₃ loadings, (e) Linear sweep voltammetry at a scan rate of 5 mV/s and (f) Chronoamperometry measurements for 15 min at applied potentials from -0.20 to -1.20V vs. RHE with a catalyst loading on the carbon paper of 0.2 mg cm⁻². The corresponding chronoamperometry measurements and UV-Vis NH₃ quantification are given in Figure S15-S20.

Figure 4a, shows the NO₃RR performance of the optimized 3xFe₂O₃/Fe-N-C catalyst (with a 0.5 mg/cm² loading on the working electrode), maintaining a FE_{NH3} above 95% over the entire -0.40 to -1.20 V potential range, again highlighting its potential independent nature towards NH₃ selectivity. This potential independent behavior on NH₃ selectivity provides an advantage in practical systems. When coupled to renewable energy, dynamic changes in the supplied energy can lead to cell voltage fluctuations. With the current system, even with cell voltage fluctuations, the product purity would remain unchanged. A maximum Yield_{NH3} of 9.2 mmol hr⁻¹ cm⁻² is achieved (*j*_{NH3} = 1,950 mA cm⁻²) at ca. 100% FE_{NH3}. To compare the performance of the 3xFe₂O₃/Fe-N-C catalyst to the current NO₃RR literature, Figure 4b compares the cathodic energy efficiency, CEE (assuming the thermodynamic reduction potential for the anodic oxygen

evolution reaction) vs. the j_{NH_3} . The CEE is a function of the FE_{NH_3} and applied potential (taking a penalty for highly cathodic potentials), while the j_{NH_3} is a function of the FE_{NH_3} and total current, enabling a comparison beyond just the FE_{NH_3} or $\text{Yield}_{\text{NH}_3}$, which can vary significantly based on the applied potential. Larger circles indicate higher concentrations of NO_3^- , often resulting in better performance, while colors are used to designate acidic, neutral, or alkaline media. The contours in Figure 4b is the product of $(\text{CEE} \times j_{\text{NH}_3})$, yielding a performance metric in terms of mA cm^{-2} , which is optimized across contours and towards the top right. From Figure 4b, it is apparent that universally, the NO_3RR suffers from relatively low energy efficiencies at meaningful j_{NH_3} (above 100 mA cm^{-2}), due to the thermodynamic reaction onset potential (0.69 V vs. RHE, $\text{pH}=14$), while more cathodic potentials (ca. -0.40 to -0.80 V) are typically required to achieve large j_{NH_3} . The majority of the NO_3RR performances in the literature report limited j_{NH_3} , less than 100 mA cm^{-2} , or utilize expensive PGM metals to realize higher j_{NH_3} , hindering industrial relevance. The $3\text{xFe}_2\text{O}_3/\text{Fe-N-C}$ catalyst (red circles) enables high current densities even at mildly reductive potentials, 297 mA cm^{-2} with a cathodic energy efficiency of ca. 33%. The potential independent nature on the NH_3 selectivity, allows the $3\text{xFe}_2\text{O}_3/\text{Fe-N-C}$ system to be operated between -0.40 to -1.20 V at near 100% FE_{NH_3} , giving ultrahigh j_{NH_3} from 297 to $1,950 \text{ mA cm}^{-2}$, outperforming the current NO_3RR literature (see Figure S21 for a linear j_{NH_3} scale).

There is significant ambiguity in determining the optimal cathodic potential to yield both an acceptable CEE and j_{NH_3} and depends on many factors including catalyst cost, device costs, CAPEX and OPEX costs, the levelized cost of NH_3 as j_{NH_3} increases and many others. To offer a semi-quantitative optimal tradeoff between energy efficiency and j_{NH_3} , Figure 4c-e offers a simplified economic analysis inspired by a recent work from Daiyan *et al.*²⁰ To construct meaningful contours, the levelized cost of NH_3 ($\$/\text{kg}$) was determined as a function of the CAPEX, OPEX and yield rates of NH_3 . These inputs consider the increasing OPEX as the cathodic potential increases, therefore decreasing energy efficiency, while also accounting for increased production rates of NH_3 (see methods for details). Three scenarios are considered, where the electricity cost varies from standard grid electricity at $\$0.07 \text{ kWh}^{-1}$ (4c), idealized renewable energy from solar power at $\$0.03 \text{ kWh}^{-1}$ (4d) and with a decreased CAPEX resulting from reduced electrolyzer stack costs (4e). From these contour plots, it's readily observed that the most effective way to cross contours (until ca. 1 A/cm^2) is through increasing the j_{NH_3} , rather than achieving low j_{NH_3} with increasing energy efficiency. This is observed for both electricity price scenarios, the lowest levelized cost of NH_3 is achieved at the most cathodic potential of -1.2 V , where the ultrahigh current density (j_{NH_3} of -1.95 A/cm^2) is achieved, despite the lower

energy efficiency. Interestingly, the impact of energy efficiency has a minor effect at small/moderate j_{NH_3} and becomes more effective at higher j_{NH_3} .

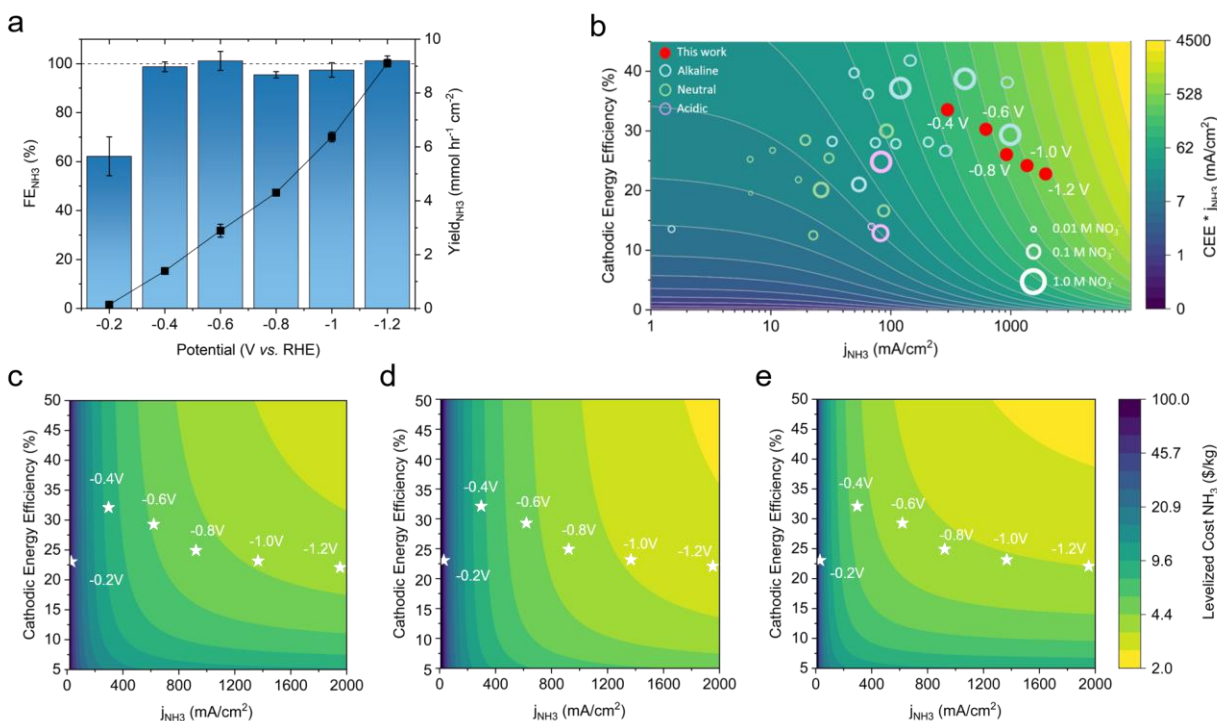


Figure 4. Electrochemical NO₃RR performance of the optimized 3xFe₂O₃/Fe-N-C catalyst with a 0.5 mg/cm² catalyst loading on the carbon paper electrode in a 1M KOH + 0.16M KNO₃ electrolyte. (a) Optimized FE_{NH₃} and Yield_{NH₃} as a function of applied potential. (b) Comparison of NO₃RR performance in the current literature, evaluating the cathodic energy efficiency vs. j_{NH_3} . Full details and references for each reported NO₃RR system are provided in Table S1. Contour plots evaluating the tradeoff of cathodic energy efficiency vs. j_{NH_3} on the levelized cost of NH₃ for cases with (c) grid electricity price, (d) idealized cost of renewable energy, and (e) reduced electrolyzer stack cost. Where performance improves across contours towards the top right corner.

Operando evaluation of Fe speciation during pre-reduction activation and electrolysis

Prior to the NO₃RR measurements, a pre-reduction activation step was performed and found to significantly improve the activity of the catalyst, as demonstrated through the LSV in Figure 5a. The pre-reduction activation applies a highly reductive potential of -1.5 V vs. RHE for 90 seconds. To elucidate the chemical state changes of the pristine 3xFe₂O₃/Fe-N-C to the now highly active catalyst, *operando* Quick XAFS was performed and complemented by post-mortem XPS. Note a milder electrolyte of 0.1M KOH + 0.016M KNO₃ (10x diluted) was used for operando experiments. Figure 5b and 5c show the XANES spectra of the Fe K-edge under

NO₃RR conditions for the 3xFe₂O₃/Fe-N-C catalyst, without and with the pre-reduction activation step, respectively. Prior to any electrochemical measurements, an initial spectrum was taken at the OCV, indicated by the gray curve. Figure S22 demonstrates that there are no significant changes between the air measurements and OCV, indicating no changes in the Fe chemical state prior to the applied potential. In Figure 5b, for the sample with no activation step, a potential of -1.0 V was directly applied, and Fe K-edge XAS spectra recorded every 3 seconds (with every two spectra being averaged for increased quality), for the first 90 seconds. Immediately, there is a distinct shift in the absorption edge toward lower energy, with a simultaneous decrease in the pre-edge feature *ca.* 7114 eV and a significant increase in the intensity of the white line. A final spectrum was acquired after 15 min of a potential hold at -1.0 V (analogous to the NO₃RR experiments discussed earlier), which demonstrates that changes in the Fe chemical state after the initial 90 seconds are relatively minor. By comparing these spectra with the Fe-reference materials, it is concluded that in the absence of a pre-reduction activation step, the NO₃RR conditions induce a transformation of Fe³⁺ to Fe²⁺. In particular, the final operando spectrum resembles strongly the Fe(OH)₂ spectrum.³³ In contrast, Figure 5c shows the evolution of Fe K-edge XAS for the catalyst, where the 90 second pre-reduction activation step at -1.5 V has been performed. In this scenario the changes in Fe K-edge XANES during the first 90 seconds are remarkably different. The white line intensity decrease is accompanied by a shift in the edge position towards a lower energy and an increase in the pre-edge feature *ca.* 7114 eV. After the 90 s of activation, a -1.0 V potential was applied (replicating the NO₃RR tests, in which an initial 90 second activation at -1.5 V is followed by -1.0 V for 15 min). The XAS spectra collected during this latter stage show a further reduction in the white line intensity and increase in the pre-edge feature, likely associated with the further reduction of Fe³⁺ (or intermediate Fe²⁺) and formation of metallic Fe (Fe⁰). These results show clearly that the evolution of chemical state of Fe is very different in cases with and without activation step (Figure S23).

To quantitatively analyze the Fe speciation observed in the *operando* Quick XAFS experiments, principal component analysis (PCA) and multivariate curve resolution (MCR) are employed and complemented by the EXAFS fitting.^{34–37} PCA and MCR methods were applied to a combined dataset, consisting of spectra collected in the experiment with and without activation step. First, PCA identified 3 spectroscopically distinct species in this combined dataset, as determined by a Scree plot (Figure S24), showing the relative importance of the principal components. Next, MCR analysis based on the alternating least squares (MCR-ALS) method was used to determine the spectra corresponding to these three species, and the corresponding

concentration profiles. For this purpose a MATLAB code developed by Jaumont et al was employed.³⁸ A successful convergence was achieved after 8 iterations. The details of the fits are shown in Table S2 and discussed in Supplementary Note 1. The 3 spectral components identified by the MCR-ALS method are shown in Figure S25. Spectral component-1 aligns well with the spectrum of metallic Fe in the Fe⁰ state. Spectral component-2 resembles the spectrum for Fe(OH)₂, and thus, can be associated with the Fe²⁺ state. Finally, spectral component-3 matches well with the 3xFe₂O₃/Fe-N-C sample and the spectrum of metallic Fe in the Fe⁰ state. Figure 5d shows the evolution of the concentration of these identified Fe species over the 15 min NO₃RR electrolysis at -1.0 V, for the 3xFe₂O₃/Fe-N-C without the pre-reduction activation. Figure 5d shows that immediately after the -1.0 V is applied, nearly all the Fe³⁺ is converted to Fe²⁺, likely in the form of Fe(OH)₂. In the following 15 min of the experiment, some Fe²⁺ is further reduced to Fe⁰, but at a very slow rate. In contrast, Figure 5e shows the concentration profiles of Fe species obtained for the case with a pre-reduction activation step. During the first 25 seconds of the 90 seconds potential hold at -1.5 V, the conversion from Fe³⁺ to Fe²⁺ is paralleled by the formation of metallic Fe⁰. During the 15 min electrolysis at -1.0 V, the remaining Fe²⁺ is further converted to Fe⁰ until ca. 550 seconds, at which point the concentration of Fe³⁺, Fe²⁺ and Fe⁰ approaches the steady state. Thus, at the highly cathodic potential of -1.5 V the reduction of Fe³⁺ to Fe⁰ is triggered, at which point the further reduction of Fe³⁺ is hindered. These results agree well with previously reported literature demonstrating that during a cathodic bias of -1.0 V, Fe oxides supported on nitrogen doped carbon were not fully reduced to Fe⁰, which was attributed to phase contractions and the insertion of H₂O in the lattice, maintaining a Fe(OH)₂ structure (Fe²⁺), despite being 560 mV lower than thermodynamically expected potential for Fe⁰.³⁹ Additionally, it has been shown that nitrogen dopants can stabilize Fe²⁺ species, preventing the complete reduction to Fe⁰ under a cathodic bias.⁴⁰ The *operando* EXAFS data in k-space shown in Figure 5f agrees with the XANES analysis, showing the clear formation of Fe⁰ during the pre-reduction activation step and further formation during the 15 min electrolysis, resembling the Fe foil reference. For the sample without the activation step, during the electrolysis, the characteristic Fe⁰ high frequency oscillations at larger k-values are also present, however, they are more less pronounced than in the case with the pre-reduction activation step. Further analysis of the EXAFS spectra in Figure S26 shows that both in the experiments with and without the activation step, a Fe-Fe bond contribution is observed. However, for the sample with the pre-reduction activation, the Fe-Fe coordination numbers are significantly larger, and the Fe-O bond distances are shorter, suggesting a larger fraction of Fe³⁺ as compared to Fe²⁺. Thus, EXAFS data analysis further

confirms the conclusions from the XANES analysis that the activated catalyst contains significant amount of Fe^{3+} species coexisting with Fe^0 (EXAFS fitting parameters given in Table S3 – S5).

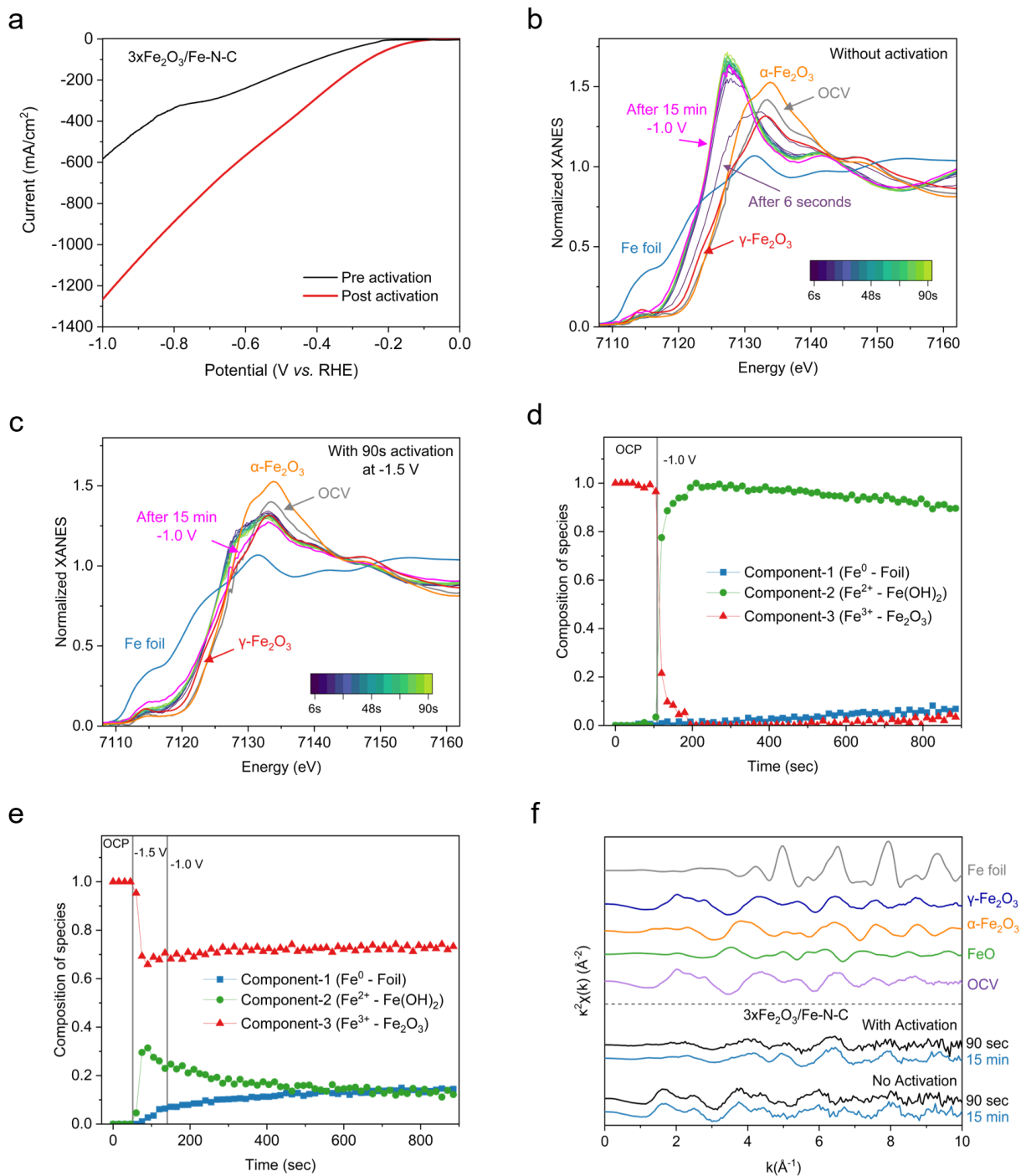


Figure 5. Operando investigation of the electronic state of Fe during the pre-reduction activation step and NO₃RR electrolysis of the 3xFe₂O₃/Fe-N-C. (a) LSV in 1M KOH + 0.16M KNO₃ demonstrating the increased activity from the pre-reduction activation step. (b) XANES spectra of the catalyst in the first 90 seconds of the NO₃RR at -1.0 V and after 15 min, for the catalyst (b) without the pre-reduction activation step and (c) with the pre-reduction activation step. Fe speciation over 15 min of NO₃RR electrolysis at -1.0 V as determined from MCR-ALS analysis of the operando XANES measurements for the catalyst (d) without the pre-reduction activation step and (e) with the pre-reduction activation step. (f) EXAFS spectra in k-space analysis of the operando measurements.

Our XAS analysis shows that even at the highly cathodic potential of -1.5 V, the complete reduction of Fe³⁺ to Fe⁰ is not observed, with a significant portion of Fe³⁺ appearing to be stabilized with the formation of Fe⁰/Fe²⁺. Furthermore, the formation and preservation of the Fe⁰ species corresponds to a significantly enhanced NO₃RR performance, which is in agreement with previous works demonstrating the effectiveness lower oxidation state Fe species towards the NO₃RR.^{41,42} The maintained Fe speciation and boosted activity are supported by a 24 hour NO₃RR electrolysis at -1.0 V, following a pre-reduction activation step. To circumvent ultrahigh NH₃ concentrations in the electrolyte and subsequent loss of NH₃ in the gas phase, the electrolysis was performed in eight 3-hour segments. Furthermore, the system was modified such that peristaltic pumps were connected an external reservoir to the working chamber, enabling a working electrolyte volume of 250 mL, with constant circulation. After a 3-hour segment, the electrolyte was sampled and refreshed. Figure 6**Error! Reference source not found.**a shows a stable current density of ca. -1.3 A/cm² at a FE_{NH₃} between 90-100% and Yield_{NH₃} of ca. 6 mmol hr⁻¹ cm⁻². The stable performance over 24 hours suggests that no further changes in Fe speciation are occurring, altering catalyst activity or selectivity to NH₃. Further highlighting the ability of the 3xFe₂O₃/Fe-N-C catalyst to preserve this ultrahigh NO₃RR performance at a near 100% FE_{NH₃}, resisting the HER even at highly reductive potentials.

To complement the *operando* quick XAFS measurements, post-mortem XPS analysis was performed on the working electrode following the pre-reduction activation step and after the 24-hour electrolysis at -1.0 V. Following the pre-reduction activation step and 24-hour electrolysis, the working electrode was dried under N₂ and stored in a gas-tight vial pre-purged with N₂ for immediate transport to the XPS. To address possible slight re-oxidation of the surface Fe during the transport of the electrode to the XPS, spectra were taken followed by quick (60 sec) Ar⁺ ion surface etch and re-sampled (see Supplementary Note 2 for details, considerations, and oxidation consequences of the Ar⁺ etching). Although not as rigorous as *operando* quick XAFS,

the deconvoluted post-mortem XPS spectra in Figure S27-S29 show a clear qualitative agreement with the XANES measurements, showing the formation of Fe^{2+} , $\text{Fe}(\text{OH})_2$ and Fe^0 during the pre-reduction activation step. Throughout the 24-hour electrolysis post-mortem XPS shows only a slight further reduction of Fe^{3+} , in agreement with the *operando* quick XAFS (first 15 min) and increased formation of Fe^0 . Following the 24-hour electrolysis, to investigate changes in the Fe_2O_3 nanoparticle structure and atomically dispersed Fe sites, atomic resolution STEM was performed, Figure 6b and 6c (and Figure S30). A slight coarsening in the Fe_2O_3 nanoparticles is observed (ca. 10 nm), however, the minor physical change in the catalyst structure does not negatively alter the NO_3RR performance as observed in Figure 6c. Additionally, at higher magnification, the coexistence of Fe_2O_3 nanoparticles and atomically dispersed Fe sites are maintained (larger images shown in Figure S31), confirming the durability of both the active Fe_2O_3 nanoparticle catalyst and active Fe-N-C support at highly reductive potentials. For better visualization of the atomically dispersed sites, a Fe-N-C catalyst without Fe_2O_3 nanoparticles after electrolysis (24 hours at -1.0 V) was imaged in Figure S32. These results are supported by other studies in the literature showing a high stability of the Fe-N-C sites under reductive potentials.^{10,27,43} Although it is critical to note that these are ex-situ measurements with the sample being exposed to air prior to imaging, which can in some cases enable the re-dispersion of single atoms agglomerated during electrolysis back to their atomically dispersed state.

From the chemical state analysis, it is hypothesized that during the pre-reduction activation step, surface Fe^{3+} species are reduced to highly active Fe^0 , which is preserved throughout the NO_3RR electrolysis maintaining the high NO_3RR activity and selectivity to NH_3 (Figure 6a). Based on this analysis, $\text{Fe}^{3+}/\text{Fe}^{2+}$ sites while active for the NO_3RR are less active than Fe^0 sites. Therefore, to maximize the NO_3RR performance, a pre-reduction step to reduce Fe^{3+} sites to Fe^0 is essential to obtain enhanced NO_3RR performance.

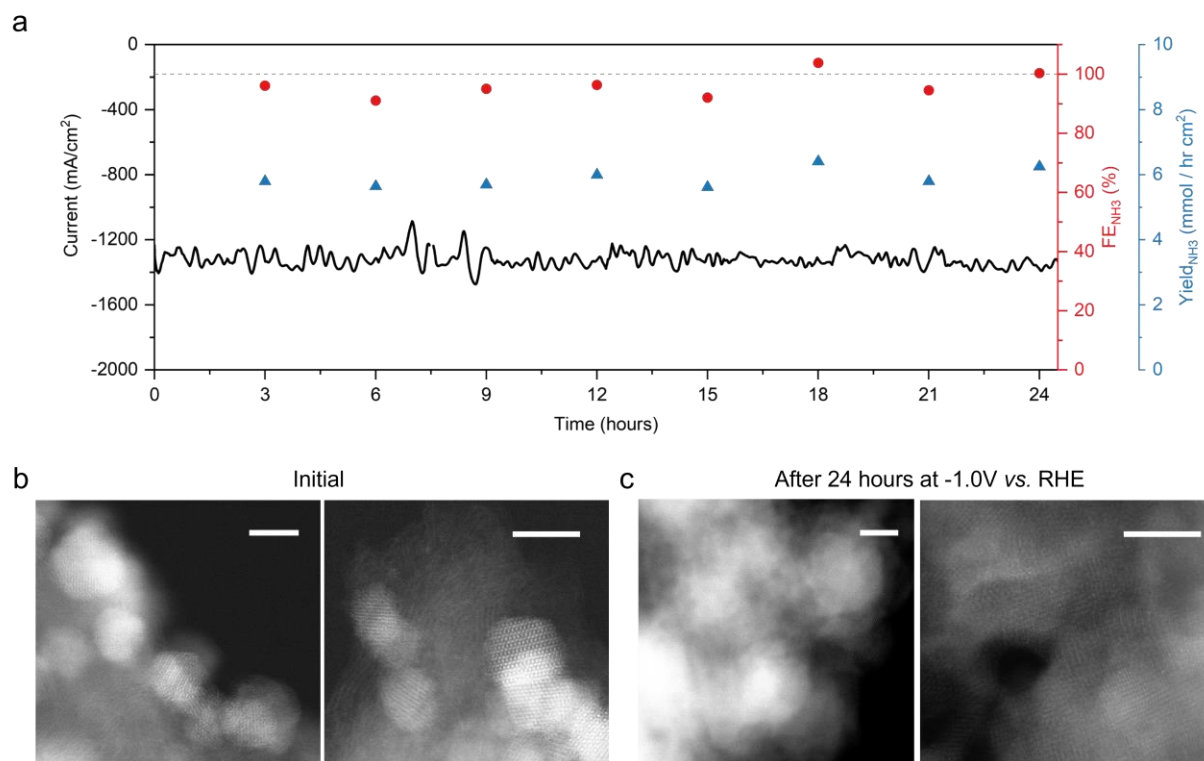


Figure 6. Durability study of the $3x\text{Fe}_2\text{O}_3/\text{Fe-N-C}$ catalyst. (a) 24-hour electrolysis at -1.0 V in $1\text{M KOH} + 0.16\text{M KNO}_3$ electrolyte. HAADF-STEM images investigating the stability of the Fe_2O_3 nanoparticles (b) for the pristine catalyst and (c) after the 24-hour electrolysis. All scale bars are 5 nm .

Conclusions

In summary, we have leveraged the high activity of Fe-based catalysts, both at the nanoparticle and single atom level, towards the selective conversion of NO_3^- to NH_3 . We synergized both the nano and atomic scales to synthesize an active particle-active support catalyst system, $\text{Fe}_2\text{O}_3/\text{Fe-N-C}$. The atomically dispersed Fe-N_x sites of the active Fe-N-C support, mixed γ/α Fe-phase, and spinel structure of the Fe_2O_3 nanoparticles was robustly confirmed employing atomic resolution STEM and EELS, XAS and XPS. The optimized $3x\text{Fe}_2\text{O}_3/\text{Fe-N-C}$ catalyst demonstrated potential independent NO_3RR activity, even at highly reductive potentials, reaching a high $\text{Yield}_{\text{NH}_3}$ of over $9\text{ mmol hr}^{-1}\text{ cm}^{-2}$ at a FE_{NH_3} of 100%, and a j_{NH_3} up to 1.95 A/cm^2 . *Operando* XANES and post-mortem XPS revealed the partial reduction of Fe^{3+} surface sites to highly active Fe^0 during the pre-reduction activation, which are maintained throughout the NO_3RR electrolysis and is critical in boosting the NO_3RR performance. A durability study at -

1.0 V over 24 hours demonstrated the robustness of the $3x\text{Fe}_2\text{O}_3/\text{Fe-N-C}$ catalyst, preserving the highly active Fe^0 sites, maintaining a current of 1.3 A/cm^2 and a FE_{NH_3} of 91-100%. This work introduces a novel active particle-active support catalyst system for the NO_3RR , utilizing a plurality of active sites at both the nanoparticle and single atom scale, to significantly enhance NO_3RR activity. While elucidating the importance of a pre-reduction activation step to create highly active surface Fe^0 species, capable of realizing NO_3^- reduction to NH_3 at industrially relevant current densities (1.95 A/cm^2) and near unity FE_{NH_3} .

Methods

Catalyst synthesis

Synthesis of Fe₂O₃, Co₃O₄ and RuO_x supported on XC72

The Fe, Co and Ru nanoparticle catalysts were synthesized using an organic solvent synthesis. Taking Fe₂O₃ as an example, first 44.8 mg of XC72 carbon and 0.2 mmol of Fe(acac)₂ was dispersed by sonication for 30 min in 40 mL of benzyl ether. Next, the mixture was deaerated by purging N₂ for 30 min. The mixture was then heated to 100 °C and then 400 μL of oleylamine and 200 μL of oleic acid were added and the temperature was held for 10 min. Next, the mixture was heated to 180 °C and 1 mL of lithium triethylborohydride was added and the temperature was held for 10 min. The catalyst mixture was then heated to 210 °C and held for 45 min. The catalyst mixture was then centrifuged and washed by ethanol before drying.

The Co and Ru based particle synthesis is identical, with the 0.2 mmol of Co(acac)₂ and Ru(acac)₂ being added in place of Fe(acac)₂.

Synthesis of Fe-N-C

The atomically dispersed Fe-N-C active support was synthesized using the sacrificial support method (SSM). First, a catalyst mixture of 6.25 g of nicarbazin, 1.25 g of OX-50 (Evonik), 1.25 g of LM150 (Cabot), 0.5 g of stöber spheres (made in house) and 0.6 g of iron (III) nitrate were added and dispersed by sonication for 30 min in water. The catalyst slurry was then dried for 24 hrs at 45 °C under continuous stirring. The partially dried slurry was then transferred to an oven for 24 hrs for complete drying at 45 °C. The catalyst mixture is then ball milled at 45 Hz for 60 min. Next, the milled catalyst powder undergoes pyrolysis in a 5% H₂ / 95% Ar atmosphere for 45 min at 975 °C. The pyrolyzed catalyst is then ball milled a second time at 45 Hz for 1 hr before being etched in a concentrated HF (18M) solution for 96 hours to remove the silica support and any nanoparticles. The etched catalyst is then washed with DI water and filtered until neutral pH before drying. A second pyrolysis under a 10% NH₃ / 90% N₂ atmosphere is performed at 950 °C for 30 min. The catalyst is then ball milled a third time at 45 Hz for 1 hr.

Synthesis of Fe₂O₃/Fe-N-C

The Fe₂O₃ nanoparticles supported on atomically dispersed Fe-N-C (Fe₂O₃/Fe-N-C) was synthesized analogously to the nanoparticle catalyst supported on XC72, with the carbon support being switched for the active Fe-N-C support.

Physical Characterization

Transmission electron microscopy (TEM) was performed on a JOEL JEM-2100F. To obtain atomic resolution images, aberration-corrected scanning transmission electron microscopy (AC-STEM) and energy dispersive X-ray spectroscopy (EDX) was performed on a JEOL ARM300CF (at 300 keV accelerating voltage). The valence state of the γ -Fe₂O₃ nanoparticles and atomically dispersed Fe sites were examined through atomic resolution electron energy loss spectroscopy (EELS) on a Nion UltraSTEM200 microscope equipped with a cold FEG, a C3/C5 aberration correction and a high-energy resolution monochromated EELS system (HERMES). To suppress beam damage, a lower accelerating voltage of 60 keV was used to collect the EELS spectra. For the spectra acquisition, the energy dispersion was set as 0.29 eV/channel at an exposure time of 500 ms/pixel. Background subtraction in the spectrum was achieved by a power-law function and the de-noising of the spectra was performed by the multivariate weighted principal component analysis (PCA) routine in the Digital Micrograph software. The smoothing of the spectra was achieved by a Savitzky-Golay method with points of window of 15 using the Origin software. For energy loss near edge structure (ELNES) analysis on Fe valence state, the spectra collected from different Fe SA locations were summed up and then averaged to improve the signal to noise ratio.

The surface valence and chemical bonds of the catalysts were analyzed by X-ray photoelectron spectroscopy (XPS) performed using a Kratos AXIS Supra spectrometer with a monochromatic Al K α source. A pass energy of 160 eV from 1400 eV to 5 eV at a step size of 1 eV was used to obtain the survey spectra. No charge neutralization was employed. CasaXPS software was used to analyze the XPS data with the spectrum being calibrated by C 1s sp² peak at (284.8 eV). For analyzing the data, two backgrounds were used, with a linear background being employed for the C 1s and N 1s spectrum, while a Shirley background was used for the N 1s and Fe 2p spectrum. For analysis of the sp² carbon, an asymmetric 50% Gaussian / 50% Lorentzian was applied. While for all other data, a 70% Gaussian / 30% Lorentzian was applied. For the Ar⁺ ion etching experiments, a survey was first taken, followed by an etch and another survey and continued in fashion. Ar⁺ ions with an energy of 5 keV were used to etch a 2 mm x 1 mm area for 60 seconds per etch cycle.

To examine the crystal phase of the catalysts, X-ray diffraction (XRD) patterns were obtained using a Rigaku Ultima-III powder X-ray diffractometer. The iron metal content of the catalysts was quantified by thermogravimetric analysis (TGA) performed on a Netzsch TG 209 F1 Libra. To

quantify the graphitic and amorphous content in the two catalyst supports (XC72 and Fe-N-C), Raman spectra were taken on an InVia, Renishaw Corp., UK system.

The ex-situ XAS measurements for the Fe₂O₃/Fe-N-C and Fe₂O₃/XC72 catalysts were performed on the SAMBA beamline at SOLEIL synchrotron radiation facility, Paris, France. The sample was measured in fluorescence mode and references in transmission mode using a Si (220) monochromator for the energy selection. Ionization chambers to measure the X-ray intensity before and after the sample were filled with a mixture of Ar/N₂ (I0) or pure Ar (I1/I2).

Operando quick XAFS measurements

The *operando* quick XAFS measurements were carried out at the P64 beamline of the Desy synchrotron radiation facility, Hamburg, Germany. A tapered undulator was used as an X-ray source. A Si(111) channel-cut single crystal monochromator was used with an oscillation frequency of 0.17 Hz. The intensity of incident X-ray radiation was measured by ionization chamber filled with pure N₂. Beam size was 0.5 x 0.5 mm². The reference and sample were measured in fluorescence mode using a PIPS detector. For the energy calibration, a γ -Fe₂O₃ reference pellet was measured before each sample measurement for 20 seconds and then moved out of the beam while the sample was moved into the beam. The *operando* measurements were performed in a home-built electrochemical single compartment cell. The electrolyte used was 0.1 M KOH with 0.016 M KNO₃. A Biologic SP300 potentiostat was used to control the potential. We performed two sets of measurements. In the first experiment, the sample was reduced at -1.5 V vs. RHE (-2.45 V vs. Ag/AgCl) for 90 seconds as an activation step and then a potential of -1.0 V vs. RHE (-1.95 V vs. Ag/AgCl) was applied and held for 15 min. In the second experiment, the potential of -1.0 V vs. RHE was applied directly without activation step.

Electrochemical measurements

Preparation of the working electrode

A carbon paper electrode (AvCarb MGL 370, Fuel Cell Store) was used as the working electrode and was cut to a geometric surface area of 0.25 cm² (0.5 x 0.5 cm). An oxygen plasma and acid treatment (0.5 M H₂SO₄) were employed to remove the PTFE layer on the electrode and increase the hydrophilicity. A catalyst ink comprised of 5 mg of catalyst, 680 μ L of isopropanol, 300 μ L of MilliQ water and 20 μ L of a 5 wt% Nafion (probe sonicated for 1 min, followed by 30 min in a

sonication bath) was drop cast on the electrode. Catalyst loading on the electrode was optimized during the study, by varying the amount of catalyst ink drop cast.

Electrochemical nitrate reduction

Electrochemical tests were performed in a customized glass H-cell (Adams & Chittenden), separated by a Celgard 3401 membrane (used as received). A three-electrode system comprising a carbon paper with catalyst, reversible hydrogen electrode (Gaskatel) and graphite rod were used as the working, reference and counter electrodes, respectively. An alkaline electrolyte, 1M potassium hydroxide (KOH) with 0.16M potassium nitrate (KNO_3) was used for the NO_3RR tests. The electrochemical cell deaerated prior to electrochemical experiments by purging N_2 gas (research grade 99.9995% - PraxAir) for 30 min at 80 sscm. During the NO_3RR , N_2 gas was continuously purged at 30 sccm. Control experiments with only 1M KOH + N_2 gas demonstrate that the catalyst is not active for N_2 reduction to NH_3 , allowing N_2 to be an inert gas in this system (Figure S14a-b). For the standard NO_3RR experiments, the working and counter electrolyte volumes are 30 mL and 25 mL, respectively. Chronoamperometric (CA) tests were performed for 15 min under vigorous stirring. Prior to CA measurements, the electrode was activated by a pre-reduction step at -1.5 V vs. RHE for 90 seconds. Linear sweep voltammetry was performed by cathodically sweeping from 0.5 to -1.0 V vs. RHE as a scan rate of 5 mV/s. Electrochemically active surface area (ECSA) was determined by varying the scan rate between 20 – 100 mV/s between 0.60 – 0.75 V vs. RHE. For the 24-hour durability test, which was segmented into eight, 3-hour sections, an electrolyte reservoir of 250 mL was connected to the cathodic chamber of the h-cell using peristaltic pumps and was continually circulated throughout the electrolysis. The large circulating reservoir prevents the buildup of produced NH_3 from becoming too high in the cell. After a 3-hour segment, all electrolyte was pumped back into the external reservoir, sampled, and then refreshed for the next 3-hour segment. The potential reported for all electrochemical tests is not iR corrected.

Isotopic (K^{15}NO_3) nitrate reduction

To confirm the N in the detected NH_3 originated from the KNO_3 feed and not from the N-doped catalyst support, the N_2 gas or other sources of contamination, NO_3RR with isotopically doped K^{15}NO_3 (99% - Cambridge Isotopes) was performed. A 1M KOH + 0.16M K^{15}NO_3 electrolyte was used. Isotopically labelled $^{15}\text{NO}_3\text{RR}$ was performed at -1.0 V vs. RHE for 15 min, after which the electrolyte was sampled and quantified by ^1H NMR. Where isotopically doped $^{15}\text{NH}_3$ yields a doublet and standard $^{14}\text{NH}_3$ results in a triplet.

Calculation of the yield and faradaic efficiency

In this study all error bars are reported based on a 90% confidence interval from a series of 3 independent measurements.

The yield rate of ammonia ($Yield_{NH_3}$) from the NO_3RR is calculated from Eq. 1.

$$Yield_{NH_3} = \frac{c_{NH_3} * V}{MW_{NH_3} * t * A_{electrode}} \quad 1$$

The Faradaic efficiency for NH_3 , FE_{NH_3} , is calculated from Eq. 2

$$FE_{NH_3} = \frac{n * F * c_{NH_3} * V}{MW_{NH_3} * Q} \quad 2$$

Where c_{NH_3} is the concentration of NH_3 in the working chamber (mg/mL), V is the volume of the working chamber (30 mL), the molar mass of ammonia, MW_{NH_3} is 17.031 g/mol, t is the electrolysis time (0.25 hours) and $A_{electrode}$ is the area of the working electrode (0.25 cm²). n is the number of electrons transferred (8e⁻ for NO_3^- to NH_3), F is Faradays constant (96,485 C) and Q is the charge passed during the electrolysis (C).

Product detection

For typical NO_3RR tests, the detection and quantification of NH_3 is achieved using a ultraviolet-visible (UV-Vis) spectrophotometer (Shimadzu, UV-2600). NH_3 was detected using the indophenol blue method in which 2 mL of electrolyte (or diluted electrolyte) is mixed with 2 mL of solution A (1M NaOH, 5 wt% salicylic acid and 5 wt% sodium citrate), 1 mL of solution B (0.05M NaClO) and solution C (1 wt% sodium nitroferricyanide). After incubating the dark at room temperature for 1 hour, the maximum absorbance is taken at ca. 655 nm and quantified with respective calibration curves. Calibration curves for the detection and quantification of $^{14}NH_3$ are given in Figure S33.

For the detection of isotopic ammonia ($^{15}NH_3$), 1H NMR is used. 3-(trimethylsilyl)-1-propanesulfonic acid sodium salt (DSS) is selected as an internal standard and Dimethylsulfoxide-d₆ (DMSO) is used as the locking solvent. The NMR spectra of a solution of 580 μ L of electrolyte, 25 μ L of DMSO, 20 μ L of 3M H_2SO_4 , and 75 μ L of 6 mM DSS is obtained on a Bruker CRYO 500

MHz spectrometer. A solvent suppression method was applied to reduce the signal of H₂O, allowing for better resolution. The spectrum was processed using the Topspin 4.0.8 software. The linear calibration for the detection and quantification of ¹⁵NH₃ are given in Figure S34.

Economic analysis – levelized cost of ammonia

To evaluate the tradeoff between energy efficiency and ammonia partial current density, the levelized cost of ammonia (LC_{NH₃}) was employed as a metric. The LC_{NH₃} is calculated analogously to Daiyan et al. and as is determined by equation 3.²⁰

$$LC_{NH_3} = \frac{R_f * CAPEX + OPEX}{Yield_{NH_3}} \quad 3$$

Where R_f is the capital recovery factor and is set at 0.08 %. $CAPEX$ is the capital cost and is solely attributed to the cost of the electrolyzer stack (in \$). $OPEX$ is the operational cost and constitutes costs associated with electricity, nitrate feed and water consumption (all in units of \$). $Yield_{NH_3}$ is the yield of ammonia (kg), giving a LC_{NH_3} in \$/kg_{NH₃}. The $Yield_{NH_3}$ is calculated based as a function of the current density and electrolyzer area (with 8e⁻ transferred per NH₃). The electrolyzer stack cost and details of the OPEX parameters are detailed below.

The electrolyzer stack cost is based on parameters in analogous economic calculations and analysis provided in a National Renewable Energy Laboratory report with a cost of \$342 kW⁻¹ operating at a cell voltage of 1.9 V and current density of 2 A/cm², which yields an assumed NO₃RR electrolyzer stack cost of 12,996 \$/m².^{20,44} In the idealized case where the stack cost can be significantly reduced, a cost of \$143 kWh⁻¹ is assumed, resulting in an electrolyzer cost of 5,434 \$/m². For the OPEX costs, the cost of the NO₃⁻ (NO_x) input is assumed to be \$315 per metric ton, as estimated in work by Jiang et al.^{20,45} The cost of water is assumed to be \$0.02 L and the cost of electricity from the grid is assumed to be \$70 MWh⁻¹ and electricity generated from renewable sources is assumed to be \$30 MWh⁻¹. The required electrolyzer area required is calculated from equation 4.

$$A_{electrolyzer} = \frac{I_{total}}{j} \quad 4$$

Where I_{total} is current passing through the electrode (A) and j is current density of the NO₃RR system. I_{total} is determined by dividing the applied power to the stack (assumed here as 1 MW) by the cell voltage (assumed here as 1.9 V). Therefore, assuming a system current density of 1.3

A/cm² (the performance demonstrated in the 24-hr electrolysis), the total required electrolyzer area is 37.6 m².

Author Information

Corresponding Author

Plamen Atanassov - Department of Chemical and Biomolecular Engineering, National Fuel Cell Research Center, University of California, Irvine, California 92697, USA

*E-mail: plamen.atanassov@uci.edu

Authors

Eamonn Murphy – Department of Chemical and Biomolecular Engineering, National Fuel Cell Research Center, University of California, Irvine, California 92697, USA

Baiyu Sun - Department of Chemical and Biomolecular Engineering, National Fuel Cell Research Center, University of California, Irvine, California 92697, USA

Martina Rüscher – Department of Interface Science, Fritz-Haber-Institut der Max-Planck-Gesellschaft, 14195 Berlin, Germany

Yuanchao Liu – Department of Chemical and Biomolecular Engineering, National Fuel Cell Research Center, University of California, Irvine, California 92697, USA

Wenjie Zang - Department of Materials Science and Engineering, University of California, Irvine, California 92697, USA

Shengyuan Guo – Department of Chemical and Biomolecular Engineering, National Fuel Cell Research Center, University of California, Irvine, California 92697, USA

Uta Hejral - Department of Interface Science, Fritz-Haber-Institut der Max-Planck-Gesellschaft, 14195 Berlin, Germany

Ying Huang - Department of Materials Science and Engineering, University of California, Irvine, California 92697, USA

Alvin Ly – Department of Materials Science and Engineering, University of California, Irvine, California 92697, USA

Iryna V. Zenyuk - Department of Chemical and Biomolecular Engineering, National Fuel Cell Research Center, University of California, Irvine, California 92697, USA

Xiaoqing Pan – Department of Materials Science and Engineering, University of California, Irvine, California 92697, USA. Department of Physics and Astronomy, University of California, Irvine, California 92697, USA

Janis Timoshenko – Department of Interface Science, Fritz-Haber-Institut der Max-Planck-Gesellschaft, 14195 Berlin, Germany

Beatriz Roldán Cuenya - Department of Interface Science, Fritz-Haber-Institut der Max-Planck-Gesellschaft, 14195 Berlin, Germany

Erik D. Spoeerke – Sandia National Laboratories, Albuquerque, New Mexico 87185, USA

Notes

The authors declare no competing financial interest.

Supporting Information

- Electrochemical performance, UV-Vis quantification, XRD, XPS, Raman, TEM, XAS fittings, catalyst loading study, electrochemical data, isotopic analysis, ECSA

Acknowledgements

This work is funded by US Department of Energy, Office of Energy Efficiency and Renewable Energy (EERE), through Advanced Manufacturing Office program to Sandia National Laboratories (AOP 34920). SNL is a multi-mission laboratory managed and operated by National Technology & Engineering Solutions of Sandia, LLC, a wholly owned subsidiary of Honeywell International, Inc., for the U.S. DOE's National Nuclear Security Administration under contract DE-NA-0003525. The views expressed in the article do not necessarily represent the views of the U.S. DOE or the United States Government. The authors acknowledge the use of facilities and instrumentation at the UC Irvine Materials Research Institute (IMRI), which is supported in part by the National Science Foundation through the UC Irvine Materials Research Science and Engineering Center (DMR-2011967).

Portions of this research were carried out at the P64 beamline at the DESY synchrotron radiation facility, Hamburg, Germany, a member of the Helmholtz Association (HGF). We would like to thank Wolfgang Caliebe for his help in performing the operando XAS measurements.

Portions of this research were carried out at the SAMBA beamline at the SOLEIL synchrotron radiation facility, Paris, France. The authors would like to sincerely thank the beamline scientists Andrea Zitolo and Emiliano Fonda for their help in performing the XAS measurements.

References

- (1) Chen, J. G.; Crooks, R. M.; Seefeldt, L. C.; Bren, K. L.; Bullock, R. M.; Darensbourg, M. Y.; Holland, P. L.; Hoffman, B.; Janik, M. J.; Jones, A. K.; Kanatzidis, M. G.; King, P.; Lancaster, K. M.; Lymar, S. V.; Pfromm, P.; Schneider, W. F.; Schrock, R. R. Beyond Fossil Fuel–Driven Nitrogen Transformations. *Science* (80-.). **2018**, *360* (6391). <https://doi.org/10.1126/science.aar6611>.
- (2) Suryanto, B. H. R.; Du, H. L.; Wang, D.; Chen, J.; Simonov, A. N.; MacFarlane, D. R. Challenges and Prospects in the Catalysis of Electroreduction of Nitrogen to Ammonia. *Nat. Catal.* **2019**, *2* (4), 290–296. <https://doi.org/10.1038/s41929-019-0252-4>.
- (3) Iriawan, H.; Andersen, S. Z.; Zhang, X.; Comer, B. M.; Barrio, J.; Chen, P.; Medford, A. J.; Stephens, I. E. L.; Chorkendorff, I.; Shao-Horn, Y. Methods for Nitrogen Activation by Reduction and Oxidation. *Nat. Rev. Methods Prim.* **2021**, *1* (1). <https://doi.org/10.1038/s43586-021-00053-y>.
- (4) Andersen, S. Z.; Čolić, V.; Yang, S.; Schwalbe, J. A.; Nielander, A. C.; McEnaney, J. M.; Enemark-Rasmussen, K.; Baker, J. G.; Singh, A. R.; Rohr, B. A.; Statt, M. J.; Blair, S. J.; Mezzavilla, S.; Kibsgaard, J.; Vesborg, P. C. K.; Cargnello, M.; Bent, S. F.; Jaramillo, T. F.; Stephens, I. E. L.; Nørskov, J. K.; Chorkendorff, I. A Rigorous Electrochemical Ammonia Synthesis Protocol with Quantitative Isotope Measurements. *Nature* **2019**, *570* (7762), 504–508. <https://doi.org/10.1038/s41586-019-1260-x>.
- (5) Choi, J.; Suryanto, B. H. R.; Wang, D.; Du, H. L.; Hodgetts, R. Y.; Ferrero Vallana, F. M.; MacFarlane, D. R.; Simonov, A. N. Identification and Elimination of False Positives in Electrochemical Nitrogen Reduction Studies. *Nat. Commun.* **2020**, *11* (1), 1–10. <https://doi.org/10.1038/s41467-020-19130-z>.
- (6) van Langevelde, P. H.; Katsounaros, I.; Koper, M. T. M. Electrocatalytic Nitrate Reduction for Sustainable Ammonia Production. *Joule* **2021**, *5* (2), 290–294. <https://doi.org/10.1016/j.joule.2020.12.025>.
- (7) Liang, X.; Zhu, H.; Yang, X.; Xue, S.; Liang, Z. Recent Advances in Designing Efficient Electrocatalysts for Electrochemical Nitrate Reduction to Ammonia. **2022**, *2200202*, 1–27. <https://doi.org/10.1002/sstr.202200202>.
- (8) Sun, J.; Alam, D.; Daiyan, R.; Masood, H.; Zhang, T.; Zhou, R.; Cullen, P. J.; Lovell, E. C.; Jalili, A.; Amal, R. A Hybrid Plasma Electrocatalytic Process for Sustainable Ammonia Production. *Energy Environ. Sci.* **2021**, *14* (2), 865–872. <https://doi.org/10.1039/d0ee03769a>.
- (9) Wang, Z.; Richards, D.; Singh, N. Recent Discoveries in the Reaction Mechanism of Heterogeneous Electrocatalytic Nitrate Reduction. *Catal. Sci. Technol.* **2021**, *11* (3), 705–725. <https://doi.org/10.1039/D0CY02025G>.
- (10) Li, P.; Jin, Z.; Fang, Z.; Yu, G. A Single-Site Iron Catalyst with Preoccupied Active Centers That Achieves Selective Ammonia Electrosynthesis from Nitrate. *Energy Environ. Sci.* **2021**, *14* (6), 3522–3531. <https://doi.org/10.1039/D1EE00545F>.
- (11) Li, J.; Zhan, G.; Yang, J.; Quan, F.; Mao, C.; Liu, Y.; Wang, B.; Lei, F.; Li, L.; Chan, A. W. M.; Xu, L.; Shi, Y.; Du, Y.; Hao, W.; Wong, P. K.; Wang, J.; Dou, S. X.; Zhang, L.; Yu, J. C. Efficient Ammonia Electrosynthesis from Nitrate on Strained Ruthenium Nanoclusters. *J. Am. Chem. Soc.* **2020**, *142* (15), 7036–7046. <https://doi.org/10.1021/jacs.0c00418>.

- (12) Hu, Q.; Qin, Y.; Wang, X.; Wang, Z.; Huang, X.; Zheng, H.; Gao, K.; Yang, H.; Zhang, P.; Shao, M.; He, C. Reaction Intermediate-Mediated Electrocatalyst Synthesis Favors Specified Facet and Defect Exposure for Efficient Nitrate-Ammonia Conversion. *Energy Environ. Sci.* **2021**, *14* (9), 4989–4997. <https://doi.org/10.1039/d1ee01731d>.
- (13) Katsounaros, I. On the Assessment of Electrocatalysts for Nitrate Reduction. *Curr. Opin. Electrochem.* **2021**, *28*, 100721. <https://doi.org/10.1016/j.coelec.2021.100721>.
- (14) Wang, Y.; Xu, A.; Wang, Z.; Huang, L.; Li, J.; Li, F.; Wicks, J.; Luo, M.; Nam, D. H.; Tan, C. S.; Ding, Y.; Wu, J.; Lum, Y.; Dinh, C. T.; Sinton, D.; Zheng, G.; Sargent, E. H. Enhanced Nitrate-to-Ammonia Activity on Copper-Nickel Alloys via Tuning of Intermediate Adsorption. *J. Am. Chem. Soc.* **2020**, *142* (12), 5702–5708. <https://doi.org/10.1021/jacs.9b13347>.
- (15) Li, L.; Tang, C.; Cui, X.; Zheng, Y.; Wang, X.; Xu, H.; Zhang, S.; Shao, T.; Davey, K.; Qiao, S. Z. Efficient Nitrogen Fixation to Ammonia through Integration of Plasma Oxidation with Electrocatalytic Reduction. *Angew. Chemie - Int. Ed.* **2021**, *60* (25), 14131–14137. <https://doi.org/10.1002/anie.202104394>.
- (16) Wang, J.; Cai, C.; Wang, Y.; Yang, X.; Wu, D.; Zhu, Y.; Li, M.; Gu, M.; Shao, M. Electrocatalytic Reduction of Nitrate to Ammonia on Low-Cost Ultrathin CoOx Nanosheets. *ACS Catal.* **2021**, *11* (24), 15135–15140. <https://doi.org/10.1021/acscatal.1c03918>.
- (17) He, W.; Zhang, J.; Dieckhöfer, S.; Varhade, S.; Brix, A. C.; Lielpetere, A.; Seisel, S.; Junqueira, J. R. C.; Schuhmann, W. Splicing the Active Phases of Copper/Cobalt-Based Catalysts Achieves High-Rate Tandem Electroreduction of Nitrate to Ammonia. *Nat. Commun.* **2022**, *13* (1), 1–13. <https://doi.org/10.1038/s41467-022-28728-4>.
- (18) Song, Z.; Liu, Y.; Zhong, Y.; Guo, Q.; Zeng, J.; Geng, Z. Efficient Electroreduction of Nitrate into Ammonia at Ultralow Concentrations Via an Enrichment Effect. *Adv. Mater.* **2022**, *34* (36). <https://doi.org/10.1002/adma.202204306>.
- (19) Deng, Z.; Ma, C.; Li, Z.; Luo, Y.; Zhang, L.; Sun, S.; Liu, Q.; Du, J.; Lu, Q.; Zheng, B.; Sun, X. High-Efficiency Electrochemical Nitrate Reduction to Ammonia on a Co₃O₄Nanoarray Catalyst with Cobalt Vacancies. *ACS Appl. Mater. Interfaces* **2022**. <https://doi.org/10.1021/acsaami.2c12772>.
- (20) Daiyan, R.; Tran-Phu, T.; Kumar, P.; Iputera, K.; Tong, Z.; Leverett, J.; Khan, M. H. A.; Asghar Esmailpour, A.; Jalili, A.; Lim, M.; Tricoli, A.; Liu, R. S.; Lu, X.; Lovell, E.; Amal, R. Nitrate Reduction to Ammonium: From CuO Defect Engineering to Waste NO_x-to-NH₃ Economic Feasibility. *Energy Environ. Sci.* **2021**, *14* (6), 3588–3598. <https://doi.org/10.1039/d1ee00594d>.
- (21) Zhou, F.; Sun, C. Nitrate-to-Ammonia Conversion on Ru/Ni Hydroxide Hybrid through Zinc-Nitrate Fuel Cell. *Small* **2022**, *18* (21). <https://doi.org/10.1002/smll.202200436>.
- (22) Qiao, Z.; Wang, C.; Li, C.; Zeng, Y.; Hwang, S.; Li, B.; Karakalos, S.; Park, J.; Kropf, A. J.; Wegener, E. C.; Gong, Q.; Xu, H.; Wang, G.; Myers, D. J.; Xie, J.; Spendelow, J. S.; Wu, G. Atomically Dispersed Single Iron Sites for Promoting Pt and Pt₃Co Fuel Cell Catalysts: Performance and Durability Improvements. *Energy Environ. Sci.* **2021**, *14* (9), 4948–4960. <https://doi.org/10.1039/d1ee01675j>.
- (23) Ly, A.; Wang, H.; Murphy, E.; Huang, Y.; Guo, S.; Liu, Y.; Zenyuk, I. V.; Atanassov, P. Electrochemical Trends of Atomically Dispersed Metal-Nitrogen-Carbon Materials As

- Oxygen Reduction Reaction Catalysts and Active Supports. *ECS Meet. Abstr.* **2022**, MA2022-01 (35), 1472. <https://doi.org/10.1149/MA2022-01351472mtgabs>.
- (24) Ao, X.; Zhang, W.; Zhao, B.; Ding, Y.; Nam, G.; Soule, L.; Abdelhafiz, A.; Wang, C.; Liu, M. Atomically Dispersed Fe-N-C Decorated with Pt-Alloy Core-Shell Nanoparticles for Improved Activity and Durability towards Oxygen Reduction. *Energy Environ. Sci.* **2020**, 13 (9), 3032–3040. <https://doi.org/10.1039/d0ee00832j>.
- (25) Murphy, E.; Liu, Y.; Matanovic, I.; Guo, S.; Tieu, P.; Huang, Y.; Ly, A.; Das, S.; Zenyuk, I.; Pan, X.; Spoecke, E.; Atanassov, P. Highly Durable and Selective Fe- and Mo-Based Atomically Dispersed Electrocatalysts for Nitrate Reduction to Ammonia via Distinct and Synergized NO₂ – Pathways. *ACS Catal.* **2022**, 12 (11), 6651–6662. <https://doi.org/10.1021/acscatal.2c01367>.
- (26) Murphy, E.; Liu, Y.; Matanovic, I.; Huang, Y.; Ly, A.; Guo, S.; Zang, W.; Yan, X.; Zenyuk, I.; Spoecke, E.; Atanassov, P. Elucidating Electrochemical Nitrate and Nitrite Reduction over Atomically-Dispersed Transition Metal Sites. *Nat. Commun.* **2023**, No. 2, 4–6. <https://doi.org/10.1038/s41467-023-40174-4>.
- (27) Wu, Z.; Karamad, M.; Yong, X.; Huang, Q.; Cullen, D. A.; Zhu, P.; Xia, C.; Xiao, Q.; Shakouri, M.; Chen, F.; Kim, J. Y.; Xia, Y.; Heck, K.; Hu, Y.; Wong, M. S.; Li, Q.; Gates, I.; Siahrostami, S.; Wang, H. Electrochemical Ammonia Synthesis via Nitrate Reduction on Fe Single Atom Catalyst. *Nat. Commun.* **2021**, 12 (1), 2870. <https://doi.org/10.1038/s41467-021-23115-x>.
- (28) Tan, H.; Verbeeck, J.; Abakumov, A.; Van Tendeloo, G. Oxidation State and Chemical Shift Investigation in Transition Metal Oxides by EELS. *Ultramicroscopy* **2012**, 116 (2012), 24–33. <https://doi.org/10.1016/j.ultramic.2012.03.002>.
- (29) Liang, L.; Jin, H.; Zhou, H.; Liu, B.; Hu, C.; Chen, D.; Wang, Z.; Hu, Z.; Zhao, Y.; Li, H. W.; He, D.; Mu, S. Cobalt Single Atom Site Isolated Pt Nanoparticles for Efficient ORR and HER in Acid Media. *Nano Energy* **2021**, 88 (May), 106221. <https://doi.org/10.1016/j.nanoen.2021.106221>.
- (30) Gao, J.; Zhou, X.; Wang, Y.; Chen, Y.; Xu, Z.; Qiu, Y.; Yuan, Q.; Lin, X.; Qiu, H. J. Exploiting the Synergistic Electronic Interaction between Pt-Skin Wrapped Intermetallic PtCo Nanoparticles and Co-N-C Support for Efficient ORR/EOR Electrocatalysis in a Direct Ethanol Fuel Cell. *Small* **2022**, 18 (25), 1–9. <https://doi.org/10.1002/smll.202202071>.
- (31) Wang, F.; Liu, X.; Jiang, B.; Zhuo, H.; Chen, W.; Chen, Y.; Li, X. Low-Loading Pt Nanoparticles Combined with the Atomically Dispersed FeN₄ Sites Supported by FeSA-N-C for Improved Activity and Stability towards Oxygen Reduction Reaction/Hydrogen Evolution Reaction in Acid and Alkaline Media. *J. Colloid Interface Sci.* **2023**, 635, 514–523. <https://doi.org/10.1016/j.jcis.2022.12.160>.
- (32) Greczynski, G.; Hultman, L. X-Ray Photoelectron Spectroscopy: Towards Reliable Binding Energy Referencing. *Prog. Mater. Sci.* **2020**, 107 (July 2019), 100591. <https://doi.org/10.1016/j.pmatsci.2019.100591>.
- (33) Situm, A.; Guo, X.; Barlow, B. C.; Guo, B.; Burgess, I. J.; Grosvenor, A. P. A Spectromicroscopy Study of the Corrosion of Polymer Coated Steel. *Corros. Sci.* **2018**, 145 (September), 35–46. <https://doi.org/10.1016/j.corsci.2018.09.008>.
- (34) Martini, A.; Borfecchia, E. Spectral Decomposition of X-Ray Absorption Spectroscopy

Datasets: Methods and Applications. *Crystals* **2020**, *10* (8), 1–46.
<https://doi.org/10.3390/cryst10080664>.

- (35) Timoshenko, J.; Haase, F. T.; Saddeler, S.; Rüscher, M.; Jeon, H. S.; Herzog, A.; Hejral, U.; Bergmann, A.; Schulz, S.; Roldan Cuenya, B. Deciphering the Structural and Chemical Transformations of Oxide Catalysts during Oxygen Evolution Reaction Using Quick X-Ray Absorption Spectroscopy and Machine Learning. *J. Am. Chem. Soc.* **2022**, No. ii. <https://doi.org/10.1021/jacs.2c11824>.
- (36) Timoshenko, J.; Frenkel, A. I. “inverting” X-Ray Absorption Spectra of Catalysts by Machine Learning in Search for Activity Descriptors. *ACS Catal.* **2019**, *9* (11), 10192–10211. <https://doi.org/10.1021/acscatal.9b03599>.
- (37) Martini, A.; Borfecchia, E.; Lomachenko, K. A.; Pankin, I. A.; Negri, C.; Berlier, G.; Beato, P.; Falsig, H.; Bordiga, S.; Lamberti, C. Composition-Driven Cu-Speciation and Reducibility in Cu-CHA Zeolite Catalysts: A Multivariate XAS/FTIR Approach to Complexity. *Chem. Sci.* **2017**, *8* (10), 6836–6851. <https://doi.org/10.1039/c7sc02266b>.
- (38) Jaumot, J.; Gargallo, R.; De Juan, A.; Tauler, R. A Graphical User-Friendly Interface for MCR-ALS: A New Tool for Multivariate Curve Resolution in MATLAB. *Chemom. Intell. Lab. Syst.* **2005**, *76* (1), 101–110.
- (39) Li, J.; Zitolo, A.; Garcés-Pineda, F. A.; Asset, T.; Kodali, M.; Tang, P.; Arbiol, J.; Galán-Mascarós, J. R.; Atanassov, P.; Zenyuk, I. V.; Sougrati, M. T.; Jaouen, F. Metal Oxide Clusters on Nitrogen-Doped Carbon Are Highly Selective for CO₂ Electroreduction to CO. *ACS Catal.* **2021**, *11* (15), 10028–10042. <https://doi.org/10.1021/acscatal.1c01702>.
- (40) Genovese, C.; Schuster, M. E.; Gibson, E. K.; Gianolio, D.; Posligua, V.; Grau-Crespo, R.; Cibin, G.; Wells, P. P.; Garai, D.; Solokha, V.; Krick Calderon, S.; Velasco-Velez, J. J.; Ampelli, C.; Perathoner, S.; Held, G.; Centi, G.; Arrigo, R. Operando Spectroscopy Study of the Carbon Dioxide Electro-Reduction by Iron Species on Nitrogen-Doped Carbon. *Nat. Commun.* **2018**, *9* (1), 1–12. <https://doi.org/10.1038/s41467-018-03138-7>.
- (41) Wagner, K. M.; Karathanasis, T.; Matocha, C. J. Reactivity of Nitrate with Zero-Valent Iron. *Water (Switzerland)* **2022**, *14* (18), 1–15. <https://doi.org/10.3390/w14182796>.
- (42) Teng, W.; Bai, N.; Liu, Y.; Liu, Y.; Fan, J.; Zhang, W. X. Selective Nitrate Reduction to Dinitrogen by Electrocatalysis on Nanoscale Iron Encapsulated in Mesoporous Carbon. *Environ. Sci. Technol.* **2018**, *52* (1), 230–236. <https://doi.org/10.1021/acs.est.7b04775>.
- (43) Lin, L.; Li, H.; Wang, Y.; Li, H.; Wei, P.; Nan, B.; Si, R.; Wang, G.; Bao, X. Temperature-Dependent CO₂ Electroreduction over Fe-N-C and Ni-N-C Single-Atom Catalysts. *Angew. Chemie - Int. Ed.* **2021**, *60* (51), 26582–26586. <https://doi.org/10.1002/anie.202113135>.
- (44) Vicker, J.; Peterson, D.; Randolph, K. Cost of Electrolytic Hydrogen Production with Existing Technology. *Department Energy United States Am.* **2020**, *5*.
- (45) Jiang, K.; Yu, H.; Chen, L.; Fang, M.; Azzi, M.; Cottrell, A.; Li, K. An Advanced, Ammonia-Based Combined NO_x/SO_x/CO₂ Emission Control Process towards a Low-Cost, Clean Coal Technology. *Appl. Energy* **2020**, *260* (x), 114316. <https://doi.org/10.1016/j.apenergy.2019.114316>.